university of groningen

University Medical Center Groningen

University of Groningen

Investigation of the Deuteron Breakup on Proton Target in the Forward Angular Region at 130 MeV

Ciepal, I.; Klos, B.; Kistryn, St.; Stephan, E.; Biegun, A.; Bodek, K.; Deltuva, A.; Epelbaum, E.; Eslami-Kalantari, M.; Fonseca, A. C.

Published in:
Few-Body systems

DOI:
10.1007/s00601-015-1014-8

IMPORTANT NOTE: You are advised to consult the publisher's version (publisher's PDF) if you wish to cite from it. Please check the document version below.

Document Version
Publisher's PDF, also known as Version of record

Publication date:
2015

Link to publication in University of Groningen/UMCG research database

Citation for published version (APA):
Ciepal, I., Klos, B., Kistryn, S., Stephan, E., Biegun, A., Bodek, K., Deltuva, A., Epelbaum, E., Eslami-Kalantari, M., Fonseca, A. C., Golak, J., Kalantar-Nayestanaki, N., Kamada, H., Khatri, G., Kirillov, D., Kirillov, D., Kliczewski, S., Kozela, A., Kravcikova, M., ... Zejma, J. (2015). Investigation of the Deuteron Breakup on Proton Target in the Forward Angular Region at 130 MeV. *Few-Body systems*, *56*(10), 665-690. https://doi.org/10.1007/s00601-015-1014-8

Copyright
Other than for strictly personal use, it is not permitted to download or to forward/distribute the text or part of it without the consent of the author(s) and/or copyright holder(s), unless the work is under an open content license (like Creative Commons).

The publication may also be distributed here under the terms of Article 25fa of the Dutch Copyright Act, indicated by the “Taverne” license. More information can be found on the University of Groningen website: https://www.rug.nl/library/open-access/self-archiving-pure/taverne-amendment.

Take-down policy
If you believe that this document breaches copyright please contact us providing details, and we will remove access to the work immediately and investigate your claim.

Downloaded from the University of Groningen/UMCG research database (Pure): http://www.rug.nl/research/portal. For technical reasons the number of authors shown on this cover page is limited to 10 maximum.

Few-Body Syst (2015) 56:665–690
DOI 10.1007/s00601-015-1014-8

I. Ciepał · B. Kłos · St. Kistryn · E. Stephan · A. Biegun
K. Bodek · A. Deltuva · E. Epelbaum · M. Eslami-Kalantari
A. C. Fonseca · J. Golak · N. Kalantar-Nayestanaki
H. Kamada · G. Khatri · Da. Kirillov · Di. Kirillov
St. Kliczewski · A. Kozela · M. Kravcikova · H. Machner
A. Magiera · G. Martinska · J. Messchendorp · A. Nogga
W. Parol · A. Ramazani-Moghaddam-Arani · B. J. Roy
H. Sakai · P. U. Sauer · K. Sekiguchi · I. Sitnik · R. Siudak
R. Skibiński · R. Sworst · J. Urban · H. Witała · J. Zejma

Investigation of the Deuteron Breakup on Proton Target in the Forward Angular Region at 130 MeV

Received: 16 February 2015 / Accepted: 1 July 2015 / Published online: 29 July 2015
© Springer-Verlag Wien 2015

Abstract A set of differential cross-section data of the ^1H(**d**, pp)n breakup reaction at 130 MeV deuteron beam energy has been measured in the domain of very forward polar angles with the use of the Germanium Wall detector at the Forschungszentrum Jülich. The data obtained for over 1000 kinematical points (112 geometries) are compared with the theoretical predictions based on various models of the three-nucleon (3N) dynamics. They comprise: the realistic nucleon-nucleon potentials alone or combined with the three-nucleon force (3NF), the coupled-channel calculations with the explicit treatment of the Δ-isobar excitation and finally, the potentials derived from chiral perturbation theory. In the part of the phase space studied, the Coulomb interaction between protons has a strong impact on the differential cross section of the breakup reaction. The strongest Coulomb effects are found in regions where the relative energy of the two protons is the smallest. In these regions the

I. Ciepał (✉) · St. Kliczewski · A. Kozela · R. Siudak
Institute of Nuclear Physics, PAS, 31342 Kraków, Poland
E-mail: izabela.ciepal@ifj.edu.pl

I. Ciepał · St. Kistryn · K. Bodek · J. Golak · G. Khatri · A. Magiera · W. Parol · R. Skibiński · R. Sworst · H. Witała · J. Zejma
Institute of Physics, Jagiellonian University, 30348 Kraków, Poland

B. Kłos · E. Stephan
University of Silesia, 40007 Katowice, Poland

A. Biegun · N. Kalantar-Nayestanaki · J. Messchendorp
KVI-CART, University of Groningen, 9747 AA Groningen, The Netherlands

M. Eslami-Kalantari
Faculty of Physics, Yazd University, Yazd, Iran

A. Ramazani-Moghaddam-Arani
Faculty of Physics, University of Kashan, Kashan, Iran

A. Nogga
Forschungszentrum Jülich, Institut für Kernphysik, 52425 Jülich, Germany

E. Epelbaum
Institut für Theoretische Physik II, Ruhr-Universität Bochum, 44780 Bochum, Germany

A. Deltuva
Institute of Theoretical Physics and Astronomy, Vilnius University, 01108 Vilnius, Lithuania

data are well reproduced exclusively by calculations which include the electromagnetic repulsion between protons. In spite of the dominance of the Coulomb force in the phase space studied, the contribution of 3NF effects is also observed.

1 Introduction

A precise description of the forces acting between nucleons is one of the most important goals of modern nuclear physics. This knowledge is fundamental for the understanding of the properties and interactions between nuclei. Properties of few-nucleon systems at low and medium energies are determined to a large extent by a pairwise nucleon-nucleon (NN) interaction. On the basis of the meson-exchange theory, which stems from Yukawa's idea [1], various models of NN forces were formed. The generation of modern realistic NN potentials like Argonne V18 [2], CD Bonn [3], Nijmegen I and II [4] reproduce the NN scattering data with an impressive precision, expressed by a χ^2 per degree of freedom very close to one. Nowadays, since QCD cannot yet be solved in the nonperturbative regime, the realistic two-nucleon (2N) potentials, together with the more sophisticated approaches like the coupled-channels (CC) method with explicit Δ-isobar excitation [5,6] and the one based on chiral perturbation theory (ChPT) [7,8], constitute a rich theoretical basis for the study of few-nucleon systems.

Direct application of the 2N potentials to the 3N systems led to discrepancies between the experimental data and the calculations. Even the most fundamental features, like the binding energies of ^{3}H and ^{3}He [9], are not reproduced in a proper way. This fact was the first clue to the existence as well as the significance of additional dynamics in 3N systems, which is referred to as the three-nucleon force (3NF). Further and more numerous indications for 3NF effects come from nucleon-deuteron (Nd) elastic scattering data [10–18]. In this case the 3NF effect was observed in the minima of the differential cross section for incoming nucleon energies larger than 60 MeV [10].

Various 3NF models [19,20] exist which are derived from meson-exchange theory and constitute improved versions of the Fujita-Myazava force [21]. The effective 3NF is also obtained within the CC framework with a Δ-isobar degree of freedom (in addition to purely nucleonic degrees of freedom). Another alternative way originates from ChPT, where the nuclear potentials are obtained by a systematic expansion in terms of momenta, and the many-body interactions appear naturally at increasing orders. The non-vanishing 3NF enters at the

P. U. Sauer
Institut für Theoretische Physik, Leibniz Universität Hannover, 30167 Hannover, Germany

A. C. Fonseca
Centro de Física Nuclear da Universidade de Lisboa, 1649-003 Lisboa, Portugal

H. Kamada
Department of Physics, Kyushu Institute of Technology, Kitakyushu 804-8550, Japan

B. J. Roy
Nuclear Physics Division, Bhabha Atomic Research Centre, Mumbai 400085, India

Da. Kirillov · Di. Kirillov · I. Sitnik
JINR, 141980 Dubna, Russia

M. Kravcikova
Technical University, 04101 Kosice, Slovakia

G. Martinska · J. Urban
P. J. Safarik University, 04154 Kosice, Slovakia

H. Sakai
University of Tokyo, Bunkyo, Tokyo 1130033, Japan

K. Sekiguchi
Tohoku University, Sendai 9808578, Japan

H. Machner
Fachbereich Physik, University Duisburg-Essen, 47048 Duisburg, Germany

next-to-next-to-leading (N2LO) order and has been used in 3N calculations, see [7,22,23]. The calculations, when compared with the rich set of elastic Nd scattering observables demonstrate the importance of 3NF effects for a proper description of the data, nevertheless they reveal discrepancies, especially in various polarization data [12,13,15,17], as well as in certain cross-section angular distributions [15,16,18]. This indicates that the 3NF models are still neglecting certain relevant ingredients. The new and rich structures of 3NF appear at next-to-next-to-next-to leading order (N3LO) of the chiral expansion. The first attempts to use consistent NN and 3N forces in 3N calculations have up to now been restricted to the ^{3}H bound state [24] and low-energy Nd scattering [25,26].

In order to probe the interaction between nucleons thoroughly, the deuteron-proton breakup reaction was chosen as a complementary tool. Investigation of this process is challenging both from the theoretical and the experimental point of view. However, it gives us an opportunity to search for a variety of dynamical effects which appear in the 3N environment.

The new generation measurement of the ^{1}H(**d**, pp)n breakup reaction, designed to study a wide phase-space region, was performed at the beam energy of 130 MeV and provided very interesting results. The comparison with the theoretical predictions revealed the significance of the 3NF in the cross-section data [27–31]. Moreover, for the configurations characterised by small polar angles and at large relative azimuthal angles φ_{12} of the emitted protons the theoretical predictions strongly underestimate the data, whereas at the small φ_{12} angles, the data are overestimated. This kind of disagreement was interpreted as a manifestation of a missing element of the dynamics, i.e. the electromagnetic long-range force was neglected in the calculations, which in principle were performed for neutron-deuteron systems.

The first calculations which included the Coulomb interaction were done with CD Bonn and CD Bonn + Δ potentials [32,33] for elastic proton-deuteron scattering. Afterwards, they were developed for the pd breakup process [34] and clearly confirmed the above hypothesis. Later, the Coulomb force was implemented into calculations with the Argonne V18 (AV18) NN potential combined with the Urbana IX (UIX) 3NF model [35].

As soon as calculations with the Coulomb interaction included became available and the database for breakup reactions was increased, Coulomb force effects were found in pd breakup cross-section data at proton beam energy as high as 135 MeV [36,37]. Here, the effects are particularly large for configurations characterized by a small relative energy between the two protons, i.e., near the proton-proton FSI configuration.

The Coulomb force effects were also studied for spin observables at deuteron beam energy of 50 and 65 MeV/nucleon [30,31,36,37]. In the region where the Coulomb effects on the cross section are important, their influence on the analyzing powers is very small. The vector analyzing power data do not reveal any sensitivity to the Coulomb force effects [38–40]. In the case of the tensor analyzing powers certain sensitivity to the electromagnetic component can be found, especially for A_{xy}, but the effect is limited to a specific region of phase space, not necessarily close to the FSI.

In order to test the calculations with the Coulomb interaction included, the phase-space region characterized by particularly sizeable Coulomb effects was chosen. A dedicated experiment was carried out at the Forschungszentrum Jülich. Studies of the ^{1}H(**d**, pp)n breakup reaction with a 130 MeV deuteron beam allowed us to extend the available database at medium energies to the very forward angular domain ($5°-14°$). The values obtained for the vector analyzing powers, A_x and A_y, are very small and do not reveal any interesting effects beyond the NN interaction [39]. On the contrary, the cross section is extremely sensitive to the Coulomb force influence [29–32]. In this paper, the theoretical predictions are compared to the new and rich set of data obtained on a systematic grid of angles and energies of the outgoing protons.

The paper is organised as follows. A description of the experimental setup and techniques is given in Sect. 2. Section 3 contains a presentation of all procedures used in the evaluation of all observables considered: event selection and energy calibration, detailed description of the detection system efficiencies, methods leading to the construction of the kinematical spectra, as well as the information about the evaluation of the differential cross section of the breakup reaction. In addition, the experimental uncertainties are also discussed. Section 4 presents a brief summary of the theoretical approaches which are used for the comparisons with the experimental results. Section 5 is dedicated to the global discussion of the results, as well as to the detailed comparisons of the data with the theoretical predictions. The summary and an outlook are given in Sect. 6.

2 Detectors and Experimental Technique

The data presented in this paper were collected in experimental runs dedicated to investigations of the breakup process ^{1}H(**d**, pp)n carried out at the Forschungszentrum Jülich, Germany. The experiments were performed

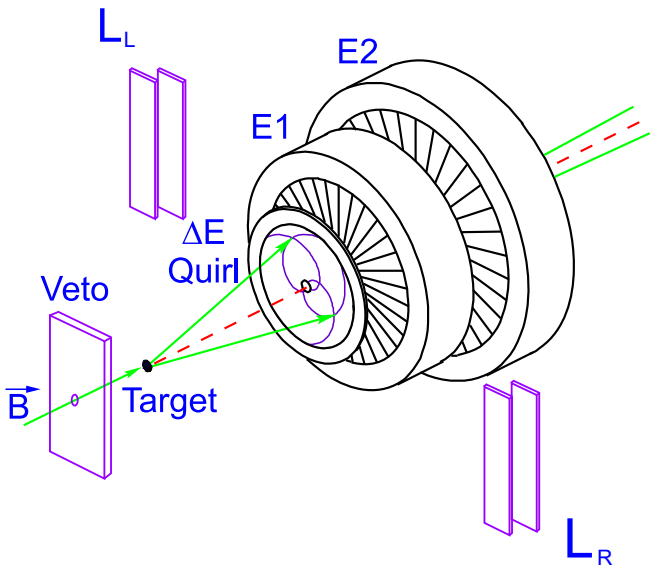

Fig. 1 (Color online) A schematic view of the *Germanium Wall* detectors and the auxiliary detectors: L_R, L_L, $Veto$. E1 and E2 refer to the two thick detectors *Pizza1* and *Pizza2*. Sizes of different elements are not to scale

Table 1 Characteristics of the *GeWall* detectors

Detector	Diameter of the hole frontside (mm)	Diameter of the hole rearside (mm)	Total diameter (mm)	Distance to the target (mm)	Thickness (mm)
Quirl	5.0	5.0	36.0	76	1.8
Pizza1	5.4	6.4	53	88.0	15.0
Pizza2	7.5	8.4	77	117.0	14.4

with an external beam of the cooler synchrotron (*COSY*) accelerator and the Germanium wall and electromagnetic spectrometer (*GEM*) system, consisting of three position sensitive high-purity germanium detectors (*HPGe*), the so-called *GeWall*, and the *Big Karl* spectrometer.

The cooler synchrotron *COSY* [41] is a storage ring device designed to accelerate beams of protons and deuterons. The ion source provides polarized and unpolarized ions of H^- and D^-, which are preaccelerated up to energies of about 45 MeV/A. Then the particles are injected into the *COSY* ring and accelerated up to the required energy. In the present case, deuterons with energy of 130 MeV were used. After the acceleration stage the beam was guided to the experimental area and focused on the target.

The *Big Karl* spectrometer was used only to transport the beam to the remote beam dump. In order to monitor the beam intensity, Dipole Exit (*DE*) counters (made of scintillator material) were used.

The target construction and operation were worked out at the Institute of Nuclear Physics (*IKP*) of the Forschungszentrum Jülich [42,43]. A cylindrical copper cell with dimensions of 6 mm diameter and 2 mm thickness was filled with liquid hydrogen. The entrance and exit windows were made of a 0.9 μm thin Mylar foil to reduce background reactions. To achieve proper pressure conditions inside the cell, a mechanical stabilization system was applied, which allowed us to attain the working pressure of 0.2 mbar at which hydrogen stays liquid in the temperature range of 14–16 K.

The charged reaction products were registered in the *GeWall* system: a set of *HPGe* detectors (*p-i-n* type) with radial symmetry with respect to the beam axis. Technical details can be found in [44] and a schematic view of the experimental arrangement is presented in Fig. 1. Two different types of detectors were used: a thin transmission detector *Quirl* with an excellent spatial resolution, and two thick detectors *Pizza 1* (*P1*) and *Pizza 2* (*P2*) for energy measurement with excellent resolution. The detectors were operated in vacuum and at liquid nitrogen temperature. Each detector possessed a central hole, to allow the beam particles which did not interact with the target to be dumped via an exit in the side yoke of the dipole of the magnetic spectrometer. The dimensions of the holes, the total diameters of the detectors and the distances from the target (see Table 1) define the angular acceptance of the detection system, which was $4°-14°$ for the polar and 2π for the azimuthal angles.

The *Quirl* detector was used to determine the position and the energy loss (ΔE-detector) of the passing particles. It was segmented on the front and the rear sides to 2×200 grooves, shaped as Archimedes spirals, each covering an angular range of 2π (including the central hole region). The bending direction of the spirals on the front (*QF*) and rear (*QR*) sides were opposite to each other. Thus, the overlaps of the spirals formed an array of about 20,000 pixels, ranging in size from $0.011\,\mathrm{mm}^2$ (the most inner) to about $0.1\,\mathrm{mm}^2$. The central hole removes approximately half of the potential crossing regions. The energy detectors *P1* and *P2* were divided into 32 segments each and were mainly used for measuring energies of the charged reaction products. Furthermore, they provided additional azimuthal information. Information on energy losses in the different *GeWall* components can be used for particle identification, whereas the sum of these energies gives the total kinetic energy of the particle. Position information from the *Quirl* detector enables the determination of all three components of the momentum vector of a particle (assuming a point-like interaction region at the target). The distance from the target and the position at *Quirl* transform directly to the azimuthal angle ϕ and the polar angle θ, see Sect. 3.1.

For experiments using the extracted beam (the experiments was placed outside the storage ring), the minimization of the beam halo is a challenge. In measurements covering the forward angular region the halo suppression becomes crucial. With the aim to suppress this effect, which otherwise induces a substantial background, electron cooling was used during the acceleration process. Finally, the deuteron beam with intensity of $2 \times 10^7/\mathrm{s}$ was focused to a spot with dimensions (rms): 1.1 mm on x- and 1.0 mm on y-axis, but the tail of the direct beam was still present on the detector. In order to decrease the trigger rate and to select the deuterons which were bombarding the center of the target, a 2 mm thick scintillating veto counter with a central hole of 4 mm diameter was mounted in front of the LH_2 cell, see Fig. 1. The signal from the veto counter was used in trigger conditions for the data-acquisition system, see Sect. 2.1.

2.1 Electronics

The signals generated by the detector elements, i.e., spirals of *Quirl* or segments of *Pizza*, were processed in a few steps. First, charge sensitive preamplifiers (*CSPA*) were used to transform the current pulses, produced in the detector by particles, into voltage signals. The output signals were split into energy and timing branches. The first one contained shaping amplifier modules coupled to *ADCs* (*Silena 3314* for the *Pizza* detectors and *Le Croy 4300B* for the *Quirl* detector, always preceded by a module *Le Croy 3309 PTQ-Peak to Charge Converter*), which finally gave the digital information on the energy deposited in the detector elements. The second branch of the circuit generated logical signals for a multiplicity analysis and a triggering system. In the case of the *Pizza* detectors this branch was equipped with fast filter amplifiers *FTA*, discriminators and *TDC* (*Time to Digital Converter*) modules. Output signals of the discriminators were sent to the trigger logic. For the *Quirl* detector branch, discriminators and *MALU* (*Multiplicity Arithmetic Logic Unit*) units were applied. The *MALU* modules clusterized neighbouring hits of the *Quirl* detector and provided information of the cluster multiplicity in each event. The trigger conditions were chosen to be:

$$T1 \equiv Quirl\ Front(1) \ \wedge \ Quirl\ Rear(1) \ \wedge \ P1(1) \ \wedge \ \overline{VETO},$$
$$T2 \equiv (Quirl\ Front(2) \vee Quirl\ Rear(2)) \ \wedge \ P1(1) \ \wedge \overline{VETO},$$

where the numbers in brackets correspond to a minimal multiplicity required in a given detector part. The *T1* was downscaled by a factor of 2^2 to enhance the coincidence rate with respect to single events. The digitized data obtained from *ADC* and *TDC* units were stored in memories and then readout by the *Data-Acquisition* system (*DAQ*).

3 Data Analysis

This Section contains a description of all steps of the data analysis procedure which leads to the final results of the breakup cross section at chosen set of kinematical configurations of the two outgoing protons. Moreover, experimental uncertainties and their sources are discussed along with the methods used for their estimation.

3.1 Reconstruction of the Particles Trajectories

The basic software for an analysis of *GeWall* data [45] comprises an energy calibration procedure and a track reconstruction package. The output of the sorter contains the full set of kinematical variables for a given

particle, like energy deposited in each detector, polar and azimuthal angles, *etc.*. This information is used in the next steps of analysis, for example to identify particles (protons and deuterons) by $\Delta E - E$ technique and to create different cuts in order to remove background events. A detailed description of the track reconstruction routine is presented in [46]. Therefore, here only a brief summary is given.

Each event is characterized by a number of clusters on every detector i.e. on *QF*, *QR*, *P1* and *P2*. The cluster consists of a group of spirals (or sectors) or of a single spiral (a sector) which registered a signal in a given event. The neighbouring channels are considered to belong to a cluster if their energy (ADC channel) is above a certain threshold, the value of which is defined for each individual channel. The energy deposited in each detector is a sum of all energies deposited in elements constituting the cluster. Besides energy, clusters are also characterized by a mean azimuthal scattering angle $\bar{\Phi}$, calculated as the weighted average of the angles of the cluster elements, i.e.:

$$E = E_1 + E_2 + \cdots + E_n, \tag{1}$$

$$\bar{\Phi} = \frac{\phi_1 \cdot E_1 + \phi_2 \cdot E_2 + \cdots + \phi_n \cdot E_n}{E_1 + E_2 + \cdots + E_n}, \tag{2}$$

where $i = 1, 2, \ldots$, n enumerates elements of the cluster, E_i is energy deposited in each element and ϕ_i is the azimuthal position of the i-th element.

Having these parameters calculated for both sides of the *Quirl* detector (*QR* and *QF*), one can identify their possible crossing points. This information is used in a track generation procedure. All the *Quirl* crossing points found are combined with the *P1* and/or *P2* clusters. Also unusual combinations like *QF/QR* and *P2* (without *P1*) are accepted. An upper limit was imposed on the difference between the relative azimuthal angles of the crossing point in the *Quirl*, *P1* and *P2* clusters. For selecting the tracks which are likely to represent real particles, additional conditions are also necessary, like a proper correspondence between values of energy deposited in *P1* and *P2*.

Several classes of events were accepted for further analysis. In the case of single-track events only events, with one cluster created in each detector were accepted, whereas for coincident events (two-track breakup events) two clusters registered in at least two detectors (*Quirl* and *P1*) were required. This selection assured an efficient reduction of accidental events. Depending on the kinetic energy of a particle, three kinds of tracks can be specified: short one (only *Quirl* detector responds), medium one (*Quirl* and *P1* respond) and long one (*Quirl*, *P1* and *P2* respond). For coincident events, combinations of the above kinds are considered. Additional combinations were defined to determine a detection efficiency.

Precise knowledge of particle emission angles is crucial for a reconstruction of the breakup and elastic scattering kinematics. For calculation of polar θ and azimuthal ϕ angles the *Quirl* detector, which provides excellent spatial resolution, was used. An active area of *Quirl* is divided on both sides into 200 Archimedes spirals, as it was presented in the previous Section. Every spiral covers an angular range of 180° and the position of the ith spiral is described with $\varphi_i = \frac{2\pi i}{200}$, which defines its angular displacement from the 0th spiral center. For any active crossing point between a left-bent (rear) and a right-bent (front) spiral, the angles φ and θ were reconstructed with a known distance between the target point and the *Quirl* detector measured by optical instruments, after the system had been evacuated.

3.2 Calibration

The energy calibration of the *GeWall* setup is a standard procedure for finding the relation between the $energy\ deposited$ and the $ADC\ channel$ for each individual detector element, i.e. spiral or segment. For this purpose the direct beam of 130 MeV deuterons with a strongly reduced intensity was used. The *GeWall* was lit up with an about one millimeter beam spot moved over the detector to obtain ADC spectra from all its elements. As it turned out during the experiment the front side of the *Quirl* detector had been slightly damaged. Therefore, for the energy determination only the rear side was used. Because of the fact that the energy deposited by 130 MeV deuterons in each *GeWall* component is known, calibration coefficients for all spirals and sectors were determined for such events. Then, the parameters obtained were used to check the reconstructed beam energy losses in the detector parts "integrated" over sectors (*P1*, *P2*) and spirals (*QR*). For the *P1* and *P2* detectors the theoretical and reconstructed beam energy losses were found to be in agreement within 1 %, whereas for the *QR* detector the deviation is about 5 %.

To improve the results, elastically-scattered deuterons and protons in a given sector of *P1* and *P2* were selected. The deuteron and proton energy loss in the *GeWall* detectors was calculated with the use of a

dedicated Monte Carlo simulation and SRIM software [47]. For each sector of *P1* and *P2* an experimental relation between the energy deposited and the polar angles of the particles was plotted separately and compared with the theoretical one. As a result, correction coefficients for each individual sector were obtained and applied to the calibration procedure. The corrections were found to be 0.7 and 3 % for *P1* and *P2*, respectively.

3.3 Identification of the Reaction Channels

In order to select the events of interest, i. e. coincident proton-proton pairs from the breakup process and deuterons or, deuteron-proton coincidences originating from the elastic scattering, the particle identification technique based on the $\Delta E - E$ dependence was applied. For that purpose energy vs. energy spectra were constructed, using different combinations of the detectors *QF/QR*, *P1*, *P2* (see Fig. 2) for the part of detector outside of the angular range of the beam-like background ($\theta > 7°$). Three groups of particles are clearly seen (Fig. 2, right panel): the long branch of the protons from the breakup reaction, the spot (or branch) of the elastically-scattered protons and, above the proton locus, the spot of the elastically-scattered deuterons together with the left-overs of the deuteron beam. Depending on the length of the track, various combinations of cuts on the $\Delta E - E$ spectra can be applied.

To identify the breakup process, two-track events with at least the *Quirl* and *P1* detectors responding in each track were selected (two, at least, medium tracks), see also Sect. 3.1. Another process of interest is elastic $d - p$ scattering, which can be registered as a single-track (deuteron or proton) or two-track events (deuteron-proton coincidences). For high-energy protons with $\theta_{prot} < 7°$, the coincident low-energy deuterons are stopped in the *Quirl* detector (event type: long track + short track). These events can be very well identified by selecting a long track of a proton on the basis of the $\Delta E(QR)$ versus $E(P1+P2)$ spectrum (see Fig. 2, right panel) together with the coplanarity condition for the coincident particles $\varphi_{pd} = \mid \varphi_{prot} - \varphi_{deut} \mid = 180°$. The dependence $\Delta E(QR)$ versus $E(P1 + P2)$ is also useful for a selection of the single-track events. The events with single protons are characteristic for the range $\theta_{prot} > 7°$, whereas the elastically-scattered high-energy deuterons are single-track events distributed over the whole detector acceptance (the coincident low-energy protons are emitted outside the detector acceptance).

For the purpose of clean selection of the elastic scattering events, further energy cuts were defined and imposed. Events corresponding to protons and deuterons were separately projected onto the *P1+P2* energy axis. Figure 3 shows examples of such projections for deuterons and protons in the selected angular ranges. The deuteron spectrum (right panel) contains two kinds of events: the scattered deuterons localized in a prominent peak and left-overs of the deuteron beam. In the proton branch (Fig. 3, left panel), the elastically-scattered protons and the protons from the breakup reaction are present. For each polar angle analogous projections were performed with the integration range of $\Delta\theta = 1°$.

In the next step the background contribution was subtracted. For the elastically scattered protons the accepted energy range was chosen between the E_a and E_b values (dashed lines in Fig. 3, left panel) and a linear dependence of the background was assumed. Due to the fact that the elastically-scattered protons

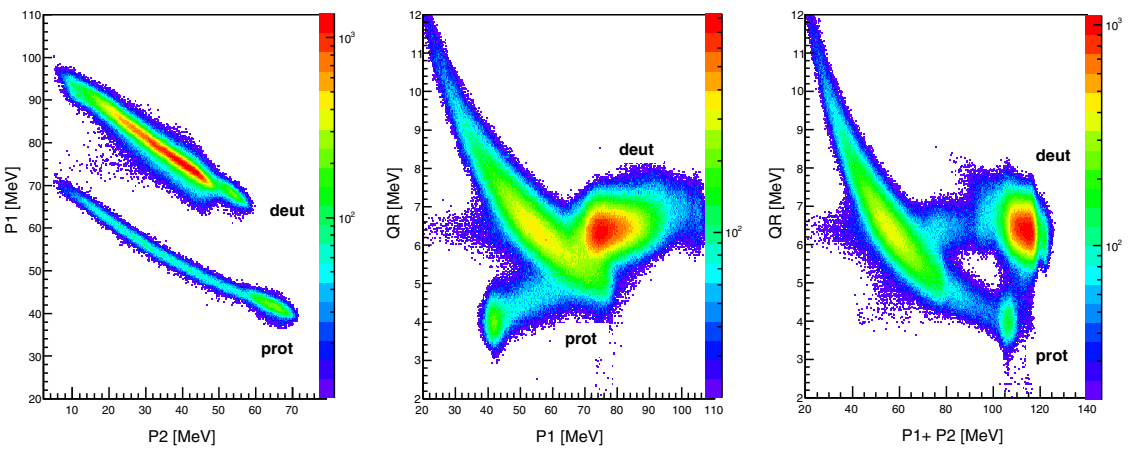

Fig. 2 (Color online) Examples of $\Delta E - E$ particle identification spectra for detector angular range of $\theta > 7°$ and for single-track events

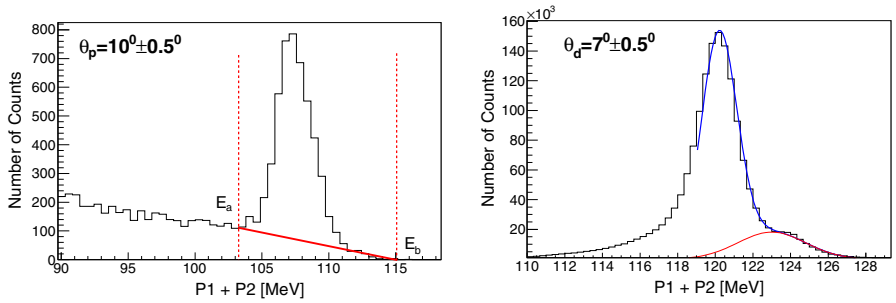

Fig. 3 (Color online) Sample spectra presenting the background subtraction methods for the elastically- scattered protons (*left panel*) and deuterons (*right panel*). The red line represents the assumed background functions

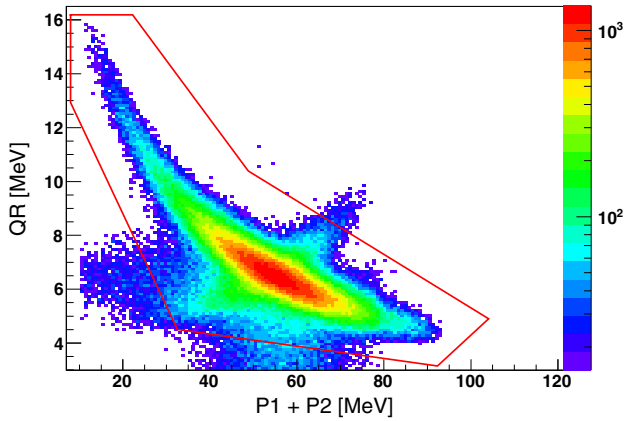

Fig. 4 (Color online) Example of the particle identification spectrum. The *lines* surrounding the area chosen identify protons from the breakup reaction

are grouped in a prominent peak riding on a continuous background of breakup events, the choice of the integration limits was not so critical. Its influence on the final result was studied, see Sect. 3.6. Protons emitted at $\theta_p < 7^\circ$ were registered as coincidences, so in this case the coplanarity condition between the two particles $\varphi_{pd} = 180^\circ \pm 30^\circ$ was also imposed.

In the case of the deuterons, background is mainly caused by the beam tail, so its energy is fixed. A typical energy distribution is shown in Fig. 3, right panel. A sum of two Gaussian functions, one with a fixed mean position and width (red curve in Fig. 3 on the right panel) was fitted to the deuteron energy distribution plot at each θ range. The background events were almost completely eliminated at polar angles above 7°.

In the case of the breakup reaction, the proton-proton pairs were chosen with an additional condition: coincidence of two medium tracks or a medium track and a long track was required, and both tracks were identified as protons, see Fig. 4. The areas defined are wide enough to avoid any losses of protons.

The geometry of coincident protons is characterized by their emission angles θ_1 and θ_2 and their relative azimuthal angle φ_{12}. In the analysis of the breakup reaction two new variables were introduced in the E_1 versus E_2 (energy of the first proton vs. energy of the second proton) plane (see Fig. 5): D denoting the distance of the (E_1, E_2) point from the theoretical kinematical curve, and S, which defines the arc-length along the kinematical locus with the starting point at the minimal E_2.

The integration ranges were $\Delta\theta_1 = \Delta\theta_2 = 2^\circ$, $\Delta\varphi_{12} = 10^\circ$ and they are wide enough to obtain good statistical accuracy. The events within each bin of $\Delta S = 4$ MeV (see an example in Fig. 5) and D-values ranging from –12 MeV to +12 MeV were projected onto the *D-axis*. The sample distribution obtained is presented in Fig. 6. For configurations characterized with the lowest value of the available angle $\theta_{min} = 5^\circ$, the distributions are contaminated by a large background contribution. This is due to the detector being overloaded by the direct beam. The spectra are smeared out and no distinguished peak can be found. Therefore, for further analysis, all events in the assumed D range are taken into account. For configurations characterized with higher theta values ($\theta > 5^\circ$), the breakup events are grouped in a prominent Gaussian shaped peak with only a low background (see Fig. 6). In this case the Gauss function was used to fit the peak. It is not clear, if all events outside of the Gaussian peak belong to the background, or if parts of them should be regarded as good events with a slightly

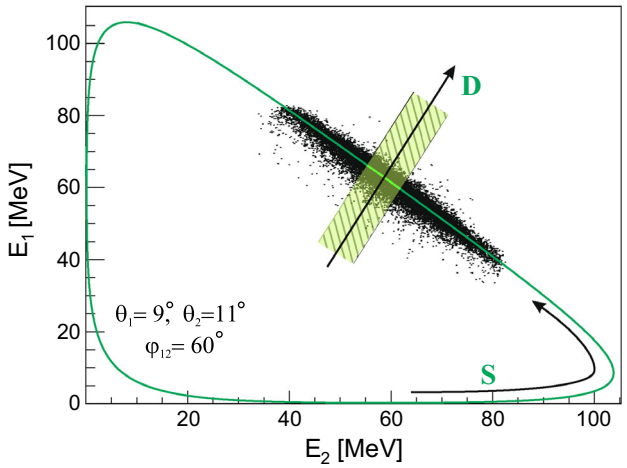

Fig. 5 (Color online) A sample E_1 *vs*. E_2 energy spectrum for a selected angular configuration of the breakup process: $\theta_1 = 9^0$, $\theta_2 = 11^0$, $\varphi_{12} = 60^0$. Variables arc-length S and distance from the D—axis are presented in a schematic way

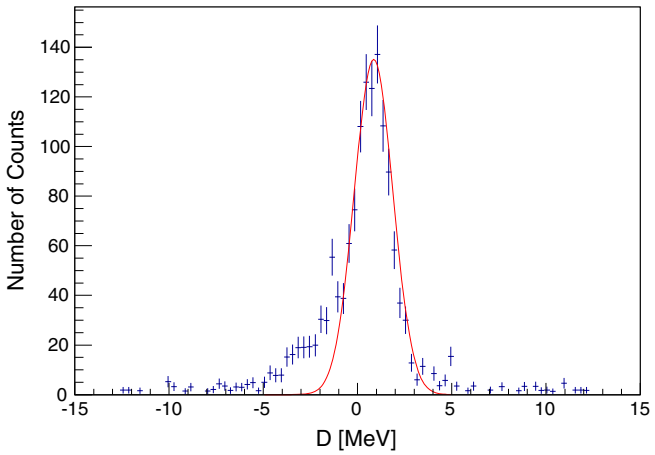

Fig. 6 (Color online) Projection of the events belonging to one ΔS bin onto the D-axis (for definition of variables see Fig. 5) in the angular region, where the detector worked correctly. The *red curve* represents the fitted Gaussian distribution

distorted energy. Therefore, two approaches were applied: integration of the peak itself or summing up of all the events in the range of -3σ and $+3\sigma$ (to treat all configurations in a consistent way). The spread of the results obtained was included in the systematic uncertainties, see Sect. 3.6 for details.

3.4 Detector Efficiency

In order to determine absolute values of the breakup cross section, it is necessary to take into account the inefficiency of the detection system and correct the numbers of the coincidences $N_{br}(S, \Omega_1, \Omega_2)$ of protons registered at the angles $\Omega_1 \equiv (\theta_1, \varphi_1)$ and $\Omega_2 \equiv (\theta_2, \varphi_2)$.

Certain spirals or sectors were inefficient or ceased to function at all ("dead" spirals). Moreover, due to the fact that the events of interest are coincidences of two particles, the clusters obtained overlap if the protons are at a very small distance from each other (for the relative azimuthal angle $\varphi_{12} \leq 60°$). The effect of "overlapping clusters" influences mostly the *Quirl* detector. To compensate the experimental counting rates for inefficiencies, the total angular range accepted by the *GeWall* was divided into cells along azimuthal and polar angles and correction factors were calculated for each cell.

3.4.1 Efficiency of the Quirl *Detector*

In the case of the *Quirl* detector the Monte Carlo simulations of the breakup process were performed with the use of the GEANT 4 package. The calculations were done for all kinematical configurations which were analysed.

In order to establish the size of the "overlapping cluster" effect and its influence on the breakup cross-section values, a model of a charge distribution on both sides of the *Quirl* detector (*QF/QR*) spirals was proposed. The radius of the spots characterizing the charge spread on the spirals R_Q was assumed to be 0.2 mm (for both sides of the detector) chosen such, that the experimental distributions of cluster hit multiplicities were reproduced. This effect contributes to the total efficiency of the *GeWall* detector for a given breakup configuration in the following way:

$$\varepsilon_Q(\Omega_1, \Omega_2) = 1 - \frac{N_1(\Omega_1, \Omega_2)}{N(\Omega_1, \Omega_2)}, \tag{3}$$

where N_1 denotes the number of the overlapping clusters, whereas N is the total number of events for a given configurations of the two protons.

3.4.2 Efficiency of the P1 *and* P2 *Detectors*

The efficiency of the *P1* detector can be easily determined by comparing the number of complete long tracks (*Quirl-P1-P2*) with incomplete long tracks (*Quirl-P2*). In order to avoid the influence of accidental *Quirl-P2* combinations, the method relies on coincidences of long tracks with medium tracks in a "reference region":

1. (Quirl − P1) − (Quirl − P1 − P2)—complete track,
2. (Quirl − P1) − (Quirl − P2)—incomplete track with missing *P1* information.

Such events can be well defined by kinematical conditions (i.e. by control of energy deposited in detector elements). The detection efficiency of *P1* is defined as follows:

$$\varepsilon_{P1}(\theta, \varphi) = \frac{N_{Q-P1-P2}(\theta, \varphi)}{N_{Q-P1-P2}(\theta, \varphi) + N_{Q-P2}(\theta, \varphi)}, \tag{4}$$

where $N_{Q-P1-P2}(\theta, \varphi)$ denotes the number of coincidences of type 1, whereas $N_{Q-P2}(\theta, \varphi)$ defines the number of coincidences of type 2. The efficiency, presented as a function of polar θ and azimuthal φ angles, generally exceeds 85 % (see Fig. 7, left panel).

In order to produce the efficiency map for the *P2* detector the elastically-scattered protons were used. They have energies large enough to pass the detector *P1* and reach the *P2* detector. Thus, the numbers of the elastically-scattered protons, identified on the basis of *QR* vs. *P1* spectra (see Fig. 2, right panel) were counted in the angular segments of $\Delta\theta = 2°$, $\Delta\varphi = 10°$ separately in two cases:

1. energy loss in the Pizza 2 detector $E(p2) = 0$: $N_{Q,P1}(\theta, \varphi)$,
2. energy loss in the Pizza 2 detector $E(p2) > 0$: $N_{Q,P1,P2}(\theta, \varphi)$.

Based on the above conditions the efficiency of *P2* was defined as follows:

$$\varepsilon_{P2}(\theta, \varphi) = \frac{N_{Q,P1,P2}(\theta, \varphi)}{N_{Q,P1,P2}(\theta, \varphi) + N_{Q,P1}(\theta, \varphi)}. \tag{5}$$

The *P2* efficiency (Fig. 7, right panel) is generally above 90 %.

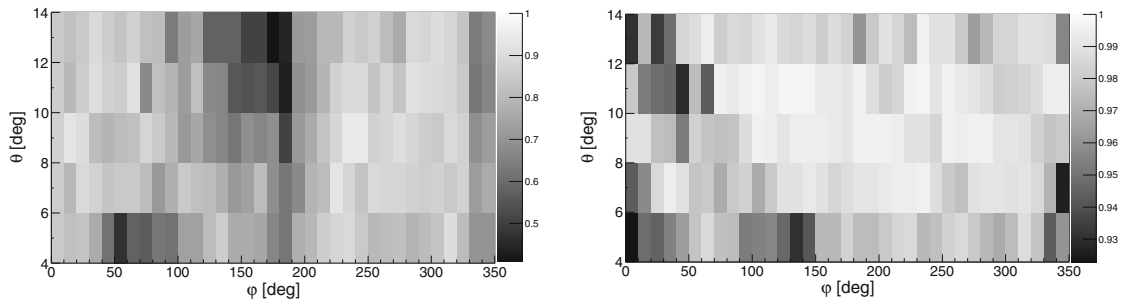

Fig. 7 Efficiency maps of the *P1* (*left panel*) and *P2* (*right panel*) detectors presented as function of polar (θ) and azimuthal (φ) angles. The range of polar angle θ is from 5° to 13° with binning of 2° and the azimuthal angle φ covers the full range, with binning of 10°

3.5 Determination of the Breakup Cross Section

Normalization of the breakup cross section was based on the known *p-d* elastic scattering cross-section data [48] and the rate of simultaneously measured elastic scattering events. Such a method ensures cancellation of factors which are difficult to determine and can be a source of systematic uncertainties (*e.g.* density or thickness of the target, collected beam charge).

Measurements with an unpolarized beam and a detector with axial symmetry allow for integration (summing up) of events over polar angles. The number of the breakup coincidences $N_{br}(S, \Omega_1, \Omega_2)$ of protons registered at given angles $\Omega_1 \equiv (\theta_1, \varphi_1)$ and $\Omega_2 \equiv (\theta_2, \varphi_2 = \varphi_1 + \varphi_{12})$ and in a S arc-length bin, is written as follows:

$$N_{br}(S, \Omega_1, \Omega_2) = \sum_{i=0}^{i=35} N_{br}\left(S, \Omega_1, \Omega_2, \varphi_1^i\right) = \frac{d^5\sigma}{d\Omega_1 d\Omega_2 dS}(S, \theta_1, \theta_2, \varphi_{12}) \cdot \Delta\Omega_1 \Delta\Omega_2 \Delta S \cdot L \cdot \varepsilon(S, \Omega_1, \Omega_2), \quad (6)$$

where the sum runs over bins of φ_1. The $\frac{d^5\sigma}{d\Omega_1 d\Omega_2 dS}$ denotes the differential cross section for the breakup reaction for a chosen angular configuration; solid angles are calculated as $\Delta\Omega_j = \Delta\theta_j \Delta\varphi_j \sin\theta_j, \quad j = 1, 2$. The events were integrated over $\Delta\theta = 2°$, $\Delta\varphi = 10°$ and $\Delta S = 4$ MeV. The $\varepsilon(S, \Omega_1, \Omega_2)$ variable contains all efficiencies and correction factors (see Sects. 3.4.1–3.4.2). L is a function of time related to the luminosity, which depends on the beam current, the density and the thickness of the target. To calculate the number of breakup coincidences and then absolute cross-section values, the integrated value of L over time of the experiment is needed. To evaluate the luminosity L, the number of elastically-scattered deuterons at a given θ angle was calculated. The number of the elastic scattering events, $N_{el}(\Omega_1^{el})$, with the deuteron registered at the angle Ω_1^{el}, is expressed by:

$$N_{el}\left(\Omega_1^{el}\right) = \sum_{i=0}^{i=35} N_{el}\left(\theta_1^{el}, \varphi_1^i\right) = \frac{d\sigma}{d\Omega_1^{el}}\left(\theta_1^{el}\right) \cdot \Delta\Omega_1^{el} \cdot L(t) \cdot \varepsilon\left(\Omega_1^{el}, E_1^{el}\right), \quad (7)$$

where the $\frac{d\sigma}{d\Omega_1^{el}}$ is the elastic scattering cross section [48], and the $\varepsilon(\Omega_1^{el}, E_1^{el})$ is related to the efficiencies and correction factors obtained with respect to the single events. The luminosity values are presented as a function of the polar angle in Fig. 8. The most forward angles, $\theta = 5°, 6°$, are not included in the analysis. This is due

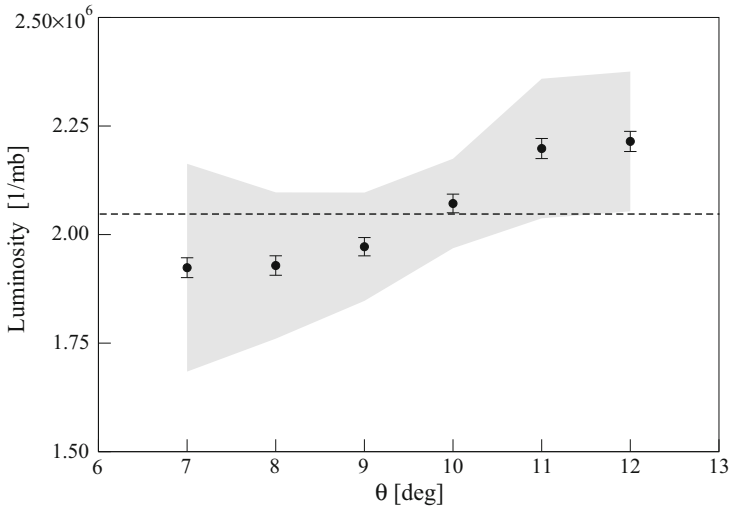

Fig. 8 Values of the luminosity presented as a function of the deuteron scattering polar angle. The *dashed line* corresponds to their weighted average

Table 2 Summary of the experimental cross-section uncertainties. The "total systematic" errors is obtained by adding the individual contributions in quadrature

Source of uncertainty	δ (%)
Statistical	
Number of elastic scattering events	2
Efficiency of *P1* and *P2*	0.1
Normalization	2
Systematic	
Energy calibration	1
Choice of integration region	1
Particle identification cuts	1
Quirl detector efficiency model	5
Background subtraction for separate slices along S	2–30
Total systematic	5.6–30.5

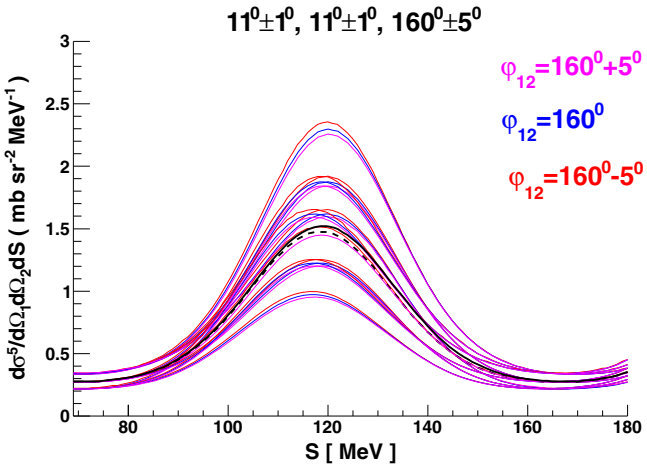

Fig. 9 (Color online) Results of the theoretical calculations with the AV18 NN potential combined with the Urbana IX 3NF and with the Coulomb interaction included (AV18+UIX+C) for chosen configuration defined in the picture. The theoretical curves marked with red, dark blue and magenta colours (or in grayscale) refer to various combinations of the θ_1, θ_2 and φ_{12} (specified in the legend) within the integration limits, which were taken into account in the averaging procedure. The *dashed black line* represents the calculations for the central configuration, whereas *the solid black* one presents the final result of the averaging approach. The differences between the *dashed* and the *solid black lines* are seen

to the large background of the direct beam at these angles, which introduces a significant systematic uncertainty related to the subtraction of the background. The angle $\theta = 13°$ was also excluded because of the large influence of the acceptance limit. For the rest of the data points the systematic uncertainties were estimated based on distributions similar to those presented in Fig. 3. The main sources of the systematical errors are the beam left-overs and deuteron energy straggling effect at polar angles larger than 7°. The final value of the luminosity was determined to be 2047520 ± 9100 (1/mb) and was calculated as a weighted average of the results for individual angles.

The formula for calculating the differential breakup cross section for a given angular configuration is expressed in terms of the luminosity L:

$$\frac{d^5\sigma}{d\Omega_1 d\Omega_2 dS}(S, \theta_1, \theta_2, \varphi_{12}) = \frac{N_{br}(S, \Omega_1, \Omega_2)}{\varepsilon(S, \Omega_1, \Omega_2) \cdot L \cdot \Delta\Omega_1 \Delta\Omega_2 \Delta S}$$

For each geometry analysed and defined by θ_1, θ_2 and ϕ_{12}, a distribution of the differential cross section as a function of S is obtained. All the results are presented in Figs. 11, 12, 13, 14, 15, 16, 17, 18.

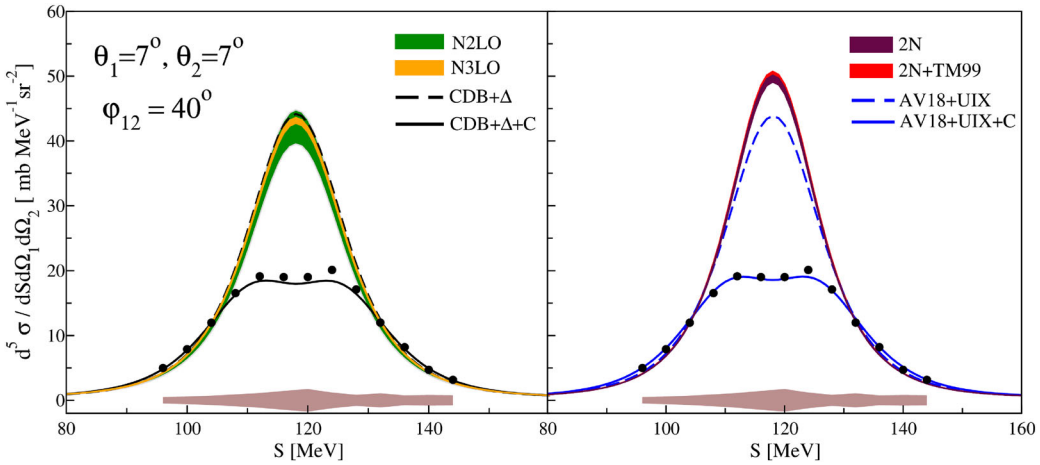

Fig. 10 (Color online) The differential breakup cross section for the configuration given by $\theta_1 = \theta_2 = 7°$ and $\varphi_{12} = 40°$. *Left panel*: Bands represent calculations based on chiral theories at N2LO (*green/dark gray*) and N3LO (*orange/light gray*), *black lines*—calculations using the coupled channel potential CD Bonn + Δ (*solid* with and *dashed* without Coulomb interaction included). *Right panel*: The same data presented with the other predictions. Bands represent calculations based on the realistic potentials with (*red/light gray*) and without 3NF (*maroon/dark gray*) included, *blue lines*—calculations based on the realistic AV18 potential combined with the Urbana IX 3NF (*dashed*) and *solid*—the same potential, but with the Coulomb force included. Bands below the cross-section distributions present the systematic uncertainties

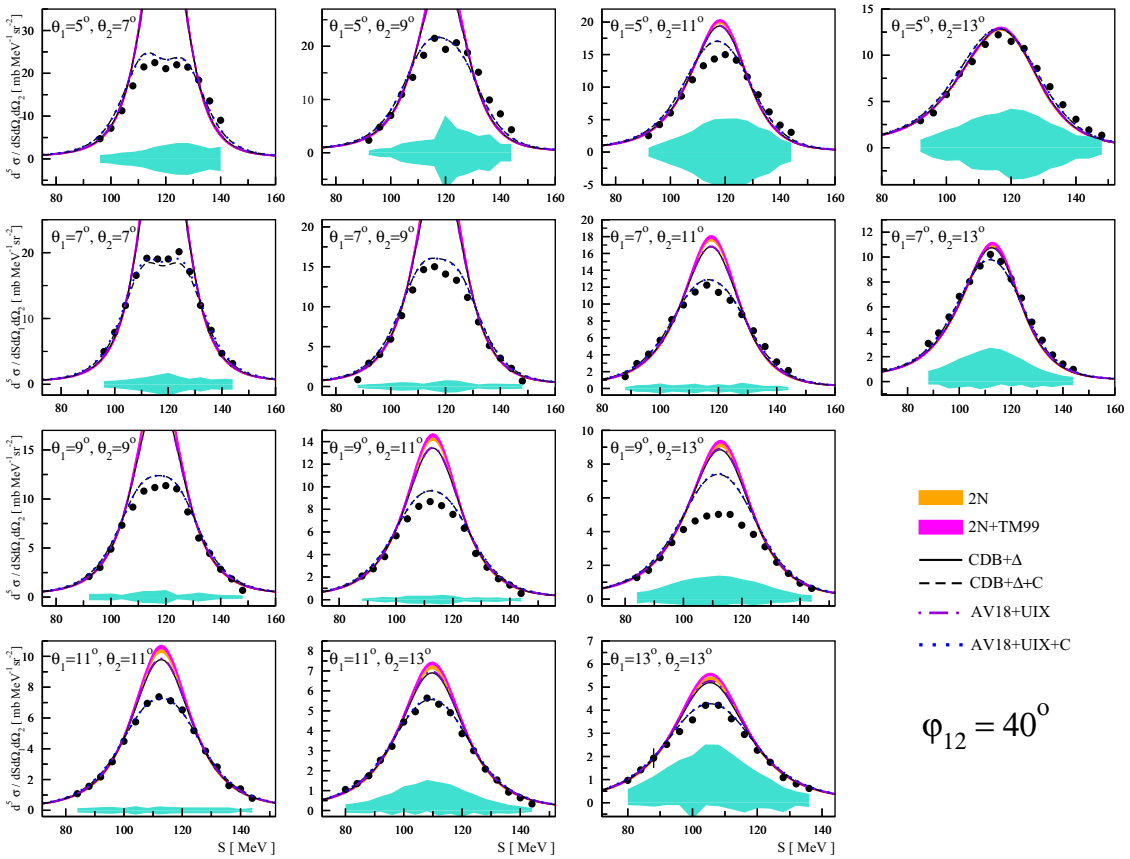

Fig. 11 Differential, integrated over S, cross-section values presented as a functions of the relative azimuthal angle φ_{12}, for pairs of the proton polar angles θ_1 and θ_2 (indicated in the *panels*). The data points are compared with the results of calculations with the AV18+UIX (*dashed lines*) and with the AV18+UIX+C (*solid lines*)

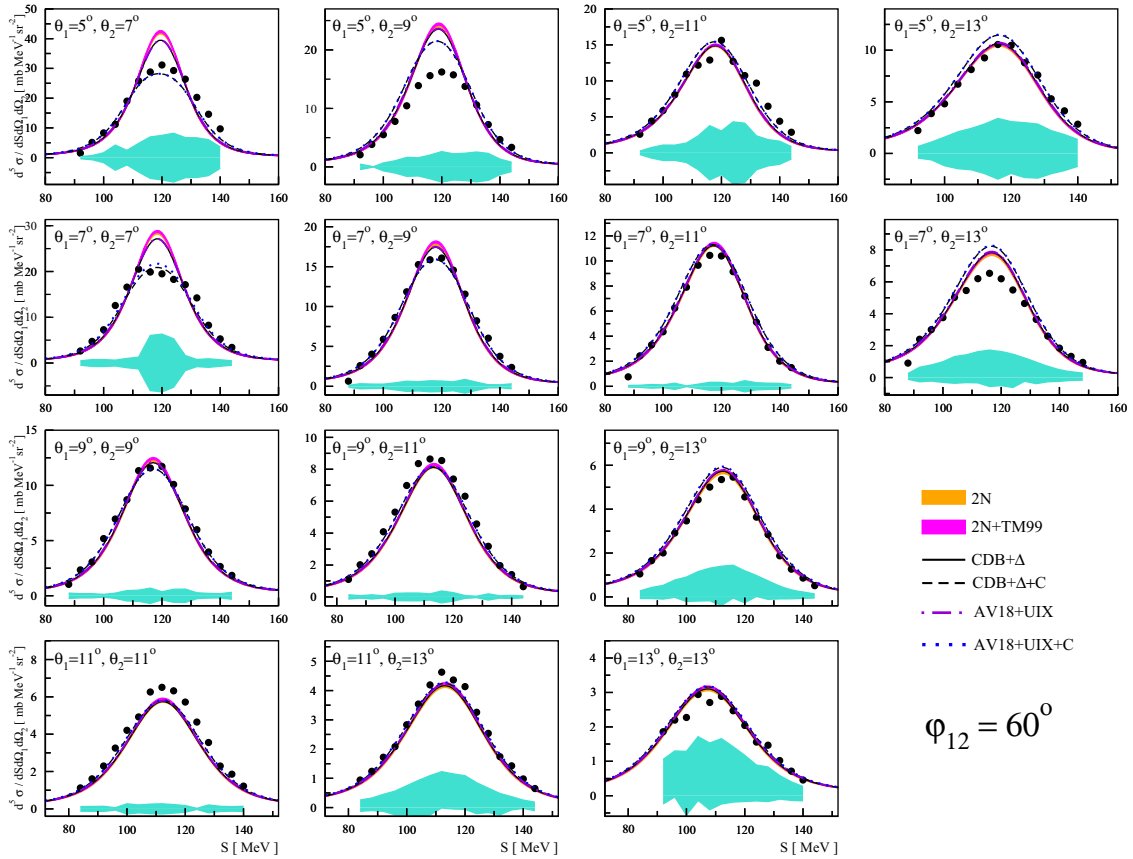

Fig. 12 (Color online) The differential breakup cross sections for the relative azimuthal angle $\varphi_{12} = 40°$ and all combinations of polar angles analyzed. *Magenta* and *orange* bands (*light gray*) represent calculations based on realistic potentials (with and without 3NF included, respectively), *black lines*—calculations using the coupled channel potential CD Bonn + Δ (*solid* with and *dashed* without Coulomb interaction included), *dashed maroon line*—calculations based on the realistic AV18 potential combined with the Urbana IX 3NF and dotted *violet line*—the same potential, but with the Coulomb force included. Turquoise (*light gray*) bands below the cross-section distributions present the systematic uncertainties

3.6 Breakup Cross Section and Experimental Uncertainties

The cross-section results are affected by statistical and systematic uncertainties and the possible sources of the errors are discussed in this section. Influence of the systematic errors was reduced significantly by detailed study of the setup geometry and the detection efficiency.

The data collected at forward angles, especially at $\theta = 5°$, suffer from a serious problem due to the detector overloading (see Sect. 3.3). The elastic scattering data (deuterons) are affected by the background of direct beam. Moreover, energy reconstruction for all particles registered at these angles is distorted, leading to difficulties in recognizing and subtracting the background. To obtain consistent results a new method of inspection and estimation of the background contribution was established.

As has been explained in Sect. 3.4 two methods of defining background were used. In the first case all events in the D-variable range from –12 MeV to +12 MeV were accepted. Alternatively, the cross section was obtained using the number of the integrated coincidences under the Gaussian peak fitted to the D-distributions, while all other data were treated as background. The Gauss function was calculated in a way to fit the right side of the D-spectrum, see Fig. 6, right panel. The final result was obtained as the average of the results obtained in both approaches, while the spread of the results defines the systematic uncertainty of the result. The systematic errors calculated according to the approach above are presented as turquoise bands below the cross-section distributions—see Figs. 11, 12, 13, 14, 15, 16, 17, 18. One can notice that for configurations defined with $\theta = 13°$ the systematic errors are asymmetric. This is due to the large systematic uncertainty of the detection efficiency factor close to the limit of the detector acceptance.

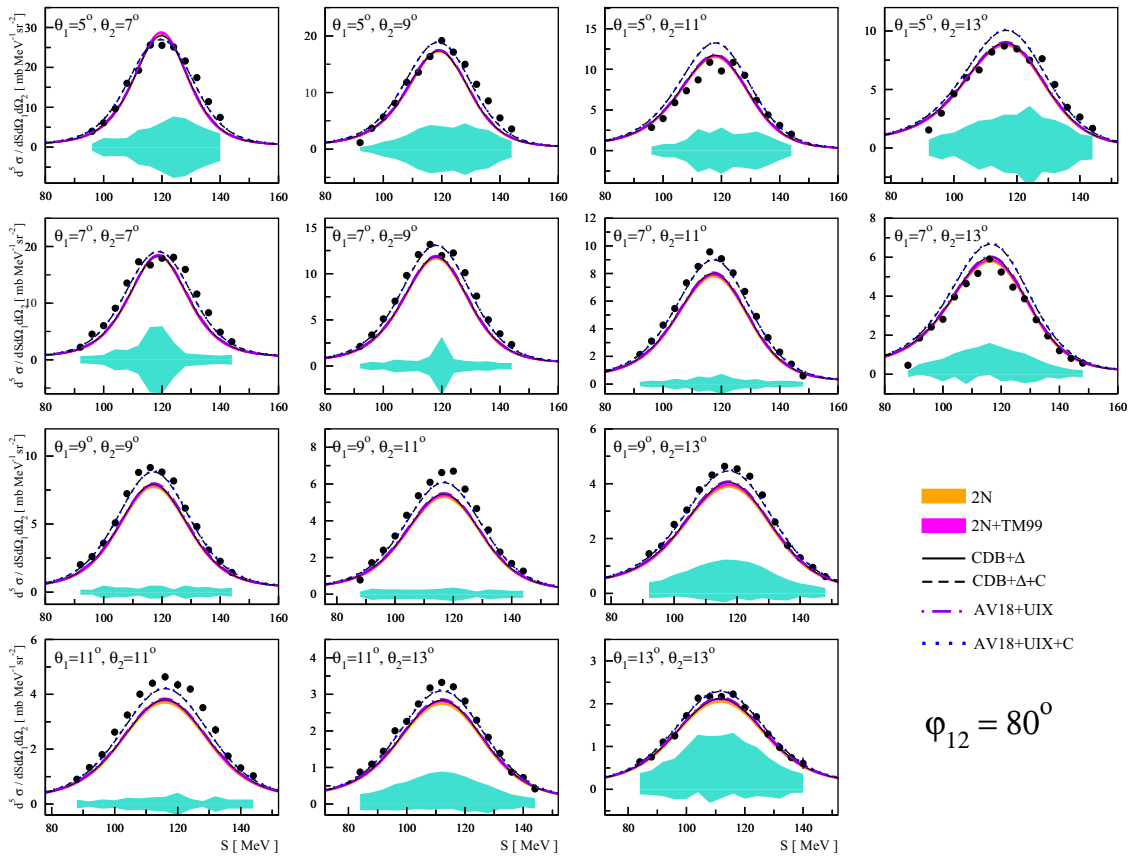

Fig. 13 (Color online) Same as in Fig. 11, but for $\varphi_{12} = 60°$

The uncertainties of the reconstruction method of the particle emission angles θ and φ originate from the uncertainty of the reaction point position, related to the thickness of the target and the size of the beam spot. The analysis of the elastic scattering events allowed for the accurate verification of the measured target-*Quirl* distance and confirmed that there is no systematic shift of the reconstructed polar angles. The angular resolution of the azimuthal angle φ is connected to the number of spirals of the *Quirl* detector (200 spirals on the both sides) and is given by the formula $\frac{2\pi}{200} \sim 0.0314$ (rad) $\sim$ 1.8°. In case of the solid angle, the accuracy varies from 10^{-6} to 10^{-5} (rad) depending on the size of the pixels.

The breakup cross section was normalized to the elastic scattering data in order to obtain absolute values. Thus, the results obtained are also affected by the error of 1.6 % quoted by Shimizu et al. [48].

The determination of the absolute values of the cross section the most significant systematic uncertainty is due to the treatment of breakup events for separate slices along the arc length S, and the associated range of the D variable. Especially for configurations defined by $\theta = 5°$, the influence of this effect is large. The other uncertainties, related to the energy calibration, the reconstruction of angles, the particle identification method and the efficiency correction also contribute, but they are much less important. Their influence on the final results has been carefully estimated and is presented in Table 2. The overall systematic errors of the breakup cross section for the majority of the configurations studied is established to be 2–30 %, depending on the geometry. The experimental uncertainties associated with the cross-section results presented in this paper are summarized in Table 2.

4 Theoretical Formalism

As has been mentioned already in Sect. 1, the calculations performed with three groups of potentials are compared with the experimental data: realistic potentials (with and without 3NF models included), realistic potentials with explicit treatment of the Δ-isobar (with and without Coulomb interaction included) and potential

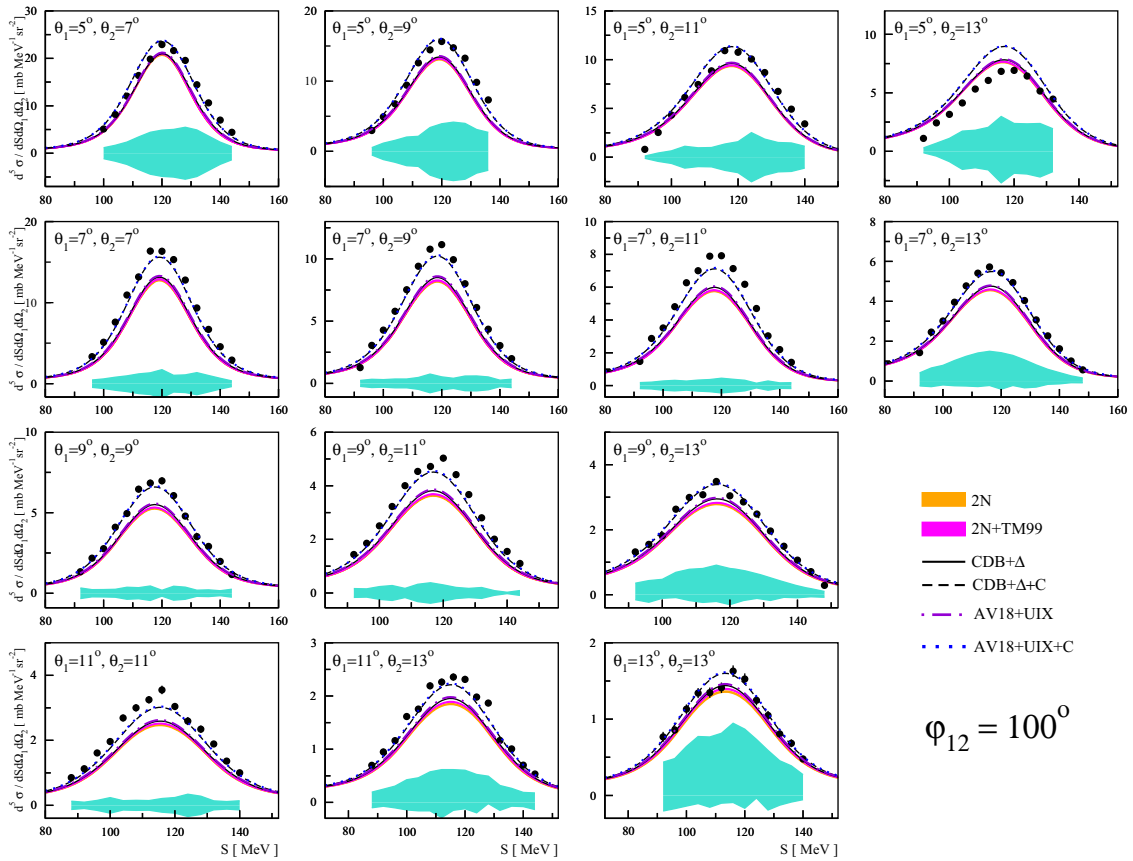

Fig. 14 (Color online) Same as in Fig. 11, but for $\varphi_{12} = 80°$

derived from ChPT. Each of the theoretical approaches offers the possibility to study different dynamical effects in the 3N systems from different points of view. The realistic potentials are coupled with the 2π-exchange TM 3NF, by taking its recent form [20] consistent with chiral symmetry, which is denoted by TM99 3NF. In case of the AV18 potential also the UIX 3NF [19] is used. The explicit inclusion of the Δ in the potential, when applied in 3N systems, leads quite naturally to 3NF graphs. The ChPT is unique from quite fundamental reasons—it is an effective field theory, but it reveals chiral behaviour consistent with QCD and a well defined hierarchical structure of orders. Moreover, it provides the possibility to estimate uncertainties of the predictions obtained. To this purpose the calculations are performed with a few combinations of the two cut-off parameters (Λ, $\tilde{\Lambda}$), which are used for regularisation of the chiral potentials. In the present work, we follow the standard approach of estimating the theoretical uncertainty by varying both cutoffs in a reasonable range. Notice however, that a new way of error estimation without relying on cut-off variations was suggested in [49]. Up to now within the ChPT framework a complete description of the NN and 3N systems has been established at the NNLO. Recently, calculations of the 2N and 3N system have been performed at the subsequent order, N3LO. However, the 3NF has not been included yet in the description of the deuteron breakup reaction at this order (restricted to only NN interaction). Furthermore, generation of chiral NN potentials up to N3LO has been introduced in [49] and extended to N4LO in [50].

The Faddeev formalism [51] allows one to calculate the observables with any of the potentials mentioned and then use the results for the interpretation in terms of nuclear force properties. This method of exact treatment of the 3N scattering problem with any short range interaction is a tool which allows to obtain the theoretical predictions with high accuracy, and not biased by (numerical) simplifications. The inclusion of the Coulomb interaction between protons into such type of calculations is one of the recent important achievements. This type of calculations "with Coulomb" are successfully performed both for the "explicit Delta" approach [32,33] and recently for the potential AV18, also when combined with UIX [35]. A more detailed description of the approaches mentioned are also available in [27,28,38].

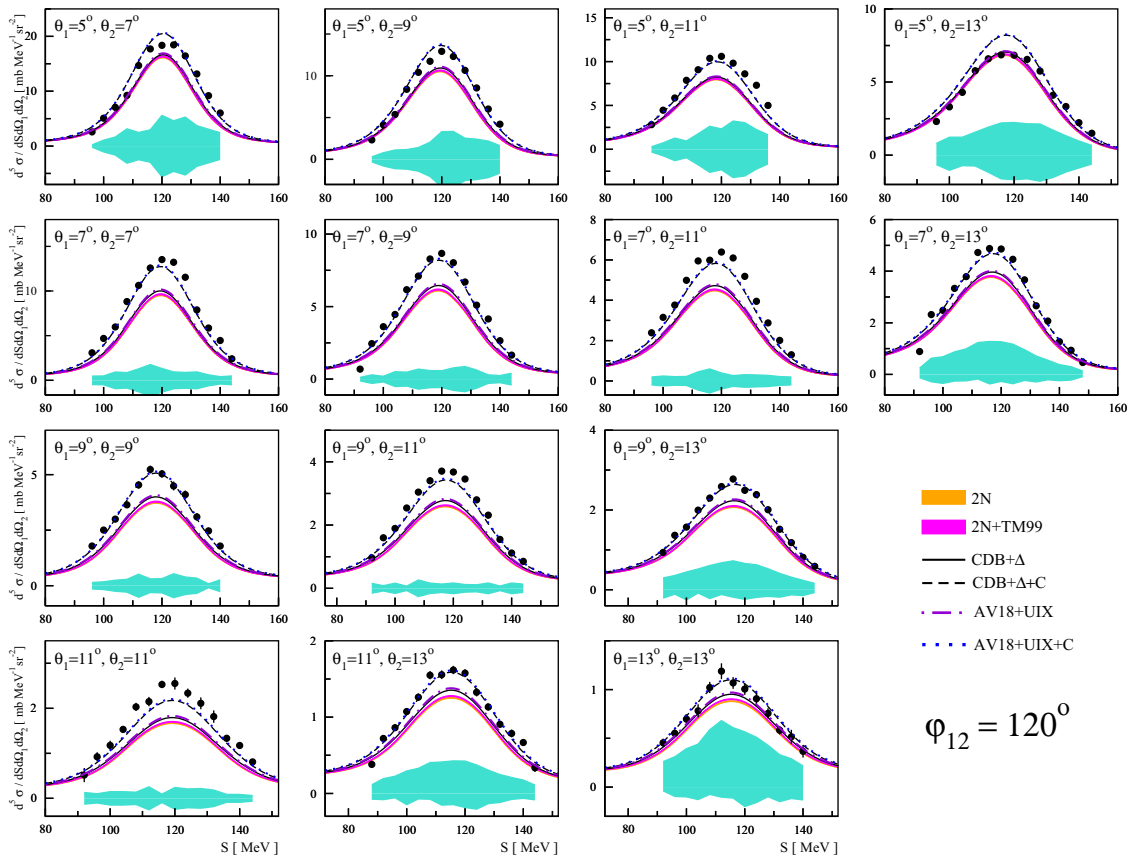

Fig. 15 (Color online) Same as in Fig. 11, but for $\varphi_{12} = 100°$

The present data are compared to a set of theoretical calculations obtained with realistic NN potentials (**2N**), NN forces combined with the TM99 3NF (**2N+TM99**), the AV18 potential combined with the UIX 3NF (**AV18+UIX**) and also with the Coulomb interaction included (**AV18+UIX+C**). In addition, calculations with the coupled-channel potential CD Bonn + Δ, neglecting (**CDB+Δ**) and including (**CDB+Δ+C**) the Coulomb force, were also used for comparisons. Moreover, the data are compared to the predictions based on the ChPT framework at two orders: **N2LO** and incomplete **N3LO** (restricted to only NN interaction).

4.1 Averaging of the Theoretical Predictions over the Integration Limits

The angular ranges defining the geometrical configurations of protons from the breakup reaction are wide enough to obtain quite good statistical accuracy, however, the results obtained are very sensitive to the averaging effects. Thus, in order to perform reasonable comparisons of the data with the theoretical models, the averaging over the same limits had to be applied to the calculated values of the cross sections. For this purpose, for each configuration given by the central values of angles θ_1^c, θ_2^c, φ_{12}^c, the cross section σ_0 values have been calculated for all combinations of angles $\theta_1^c \pm \frac{1}{2}\Delta\theta_1$, $\theta_2^c \pm \frac{1}{2}\Delta\theta_2$, $\varphi_{12}^c \pm \frac{1}{2}\Delta\varphi_{12}$ and the central values, with the step of 1 MeV in the variable S. There was, however, one exception regarding the configurations defined by the central values of the polar angles equal to 13°. Due to the detection system acceptance (the highest available values of the polar angle is 13.5°) the calculations for this geometry were performed within the ranges of the polar angles $\theta_1^c = 13^{+0.5°}_{-1°}$, $\theta_2^c = 13^{+0.5°}_{-1°}$.

The theoretical cross-section values were multiplied by the solid angle factor, then the data were placed on the E_2 *versus* E_1 plane and projected onto the curve corresponding to relativistic kinematics, calculated for the central geometry (θ_1^c, θ_2^c, φ_{12}^c). The importance of the averaging procedure is demonstrated in Fig. 9. This approach to averaging of the theoretically calculated cross sections is equivalent to event integration within the ranges accepted in the analysis. The procedure applied also projects the results of non-relativistic

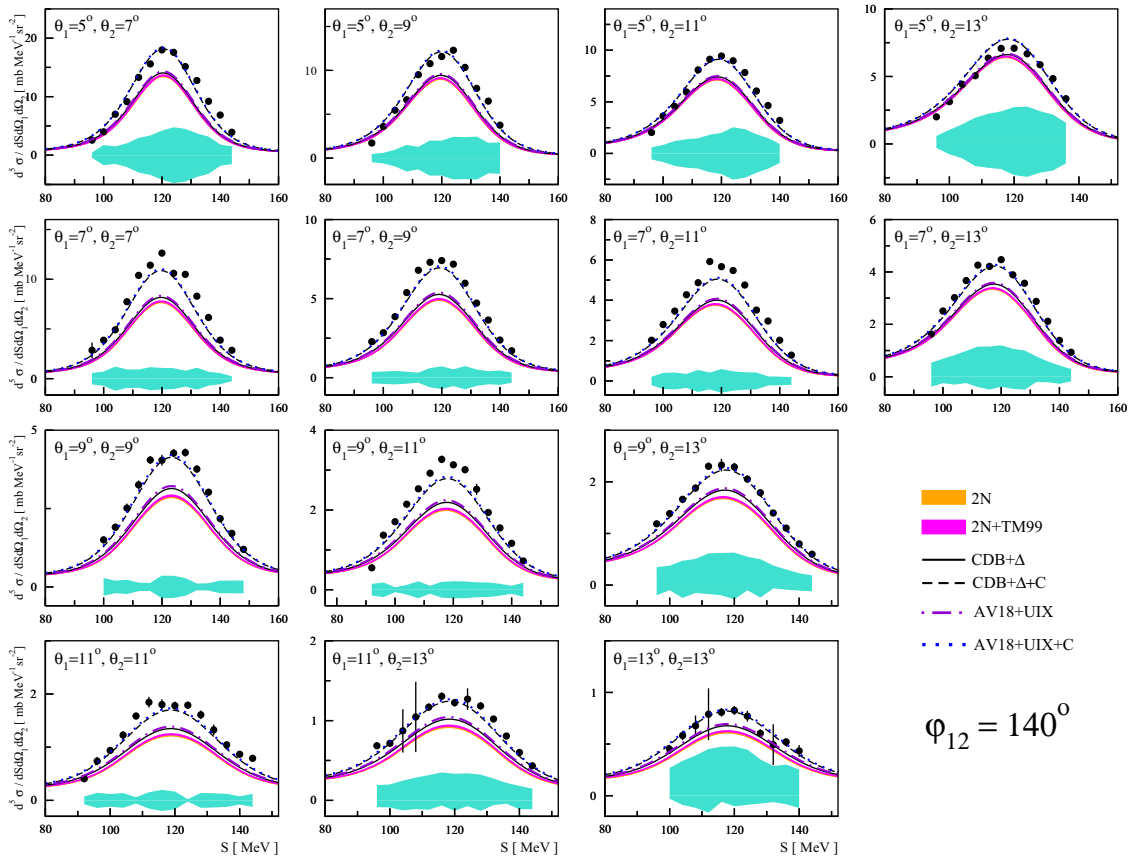

Fig. 16 (Color online) Same as in Fig. 11, but for $\varphi_{12} = 120°$

calculations onto relativistic kinematics. In this way they can be directly compared to the S distributions of the data, without the necessity to correct for the difference of arc-lengths calculated along relativistic and non-relativistic kinematic curves.

5 Results

Experimental cross-section data are obtained for 112 geometries of the two protons from the breakup reaction. Polar angles θ_1 and θ_2 are varied between 5° and 14° with the step size of 2° and their relative azimuthal angle φ_{12} is taken in the range from 40° to 180°, with the step size of 20°. The experimental results were integrated within the ranges of $\Delta\theta_1 = \Delta\theta_2 = 2°$ and $\Delta\varphi_{12} = 10°$ for each combination of the central values θ_1, θ_2 and φ_{12} (with exception of $\theta_i = 13°$, where the range of $12°-13.5°$ is accepted). The bin size along the kinematic curve S was chosen to be 4 MeV. The choice of the event integration limits provided sufficient statistical accuracy to permit discrimination between the quality of the descriptions of the theoretical predictions. The results for all individual configurations are given in Figs. 11, 12, 13, 14, 15, 16, 17, 18. They are presented in comparison with the state-of-the-art theoretical calculations (see Sects. 1, 4). The results presented as bands reflect the spread of the results of calculations obtained with the realistic potentials: CD Bonn, AV18, Nijm I and Nijm II. In a similar way the 2N potentials complemented with the TM99 3NF are presented. The ChPT results are also shown as bands, but in this case the width of the band represents the theoretical uncertainty associated with the calculations. The remaining approaches are shown as lines. The brown (light gray) bands at the bottom of the cross-section distributions represent the systematic errors, see Sect. 3.6 for details. Since the predictions represented as bands (2N, 2N+TM99, N2LO and N3LO) are often overlapping, the N2LO and N3LO were removed from the Figs. 11, 12, 13, 14, 15, 16, 17, 18 to clarify the pictures. In Fig. 10 one can see an example of the full set of the theories, divided into two parts.

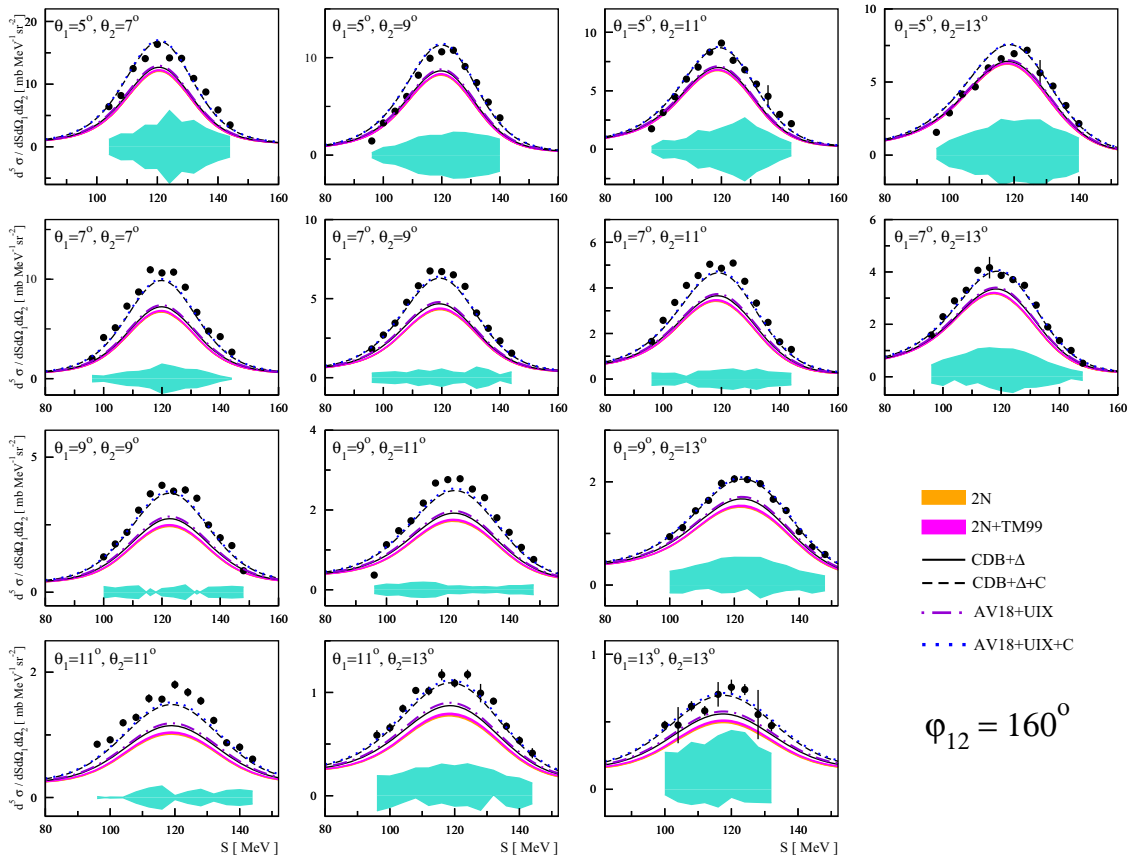

Fig. 17 (Color online) Same as in Fig. 11, but for $\varphi_{12} = 140°$

The importance of including the Coulomb force for a proper description of the experimental data demonstrates itself in specific configurations of the polar and azimuthal angles as already visible in the cross-section distributions in Figs. 11, 12, 13, 14, 15, 16, 17, 18. Therefore, the cross-section data integrated over S were studied as a function of the φ_{12} variable. The same integration, limited by the experimental energy threshold of 30 MeV, was done for the model predictions. The results for all the analysed combinations of θ_1, θ_2 are shown in Fig. 19. The integrated experimental cross sections are compared to the correspondingly integrated theoretical data based on the AV18+UIX (dashed black lines) and AV18+UIX+C (solid black lines) models. The present investigations confirm the global picture of the crucial role of the Coulomb force.

The calculations which neglect the Coulomb force usually overestimate the data at the lowest relative azimuthal angle ($\varphi_{12} = 40°$), while for $\varphi_{12} = 60°$ the predictions and the data are in agreement. In the region characterised with higher $\varphi_{12} \geq 80°$, the calculations are underestimating the data. Such a behavior is consistent with the intuitive understanding (neglecting any interference of the dynamical ingredients)—the Coulomb repulsion decreases the number of protons in configurations with small relative energies. This corresponds to a situation when the protons stay close together for a relatively long time and the repulsion can lead to a significant change of their initial trajectories. With growing φ_{12} the discrepancy changes sign and becomes smaller. At a certain point the theoretical curves intersect. This refers to a situation when the number of "incoming" and "outgoing" protons is balanced and the net effect of the Coulomb force is equal to zero. In a range of the higher relative angles the number of protons is increased. This, in turn, is caused by the protons originating from the region where the repulsion is strong.

In order to quantitatively inspect the description of the whole data set provided by various models and to identify regions where some interesting effects or problems exist, the value of χ^2 per degree of freedom (d.o.f.) has been calculated for all 112 configurations (about 1360 cross-section data points). Such global χ^2 studies allow one to conclude on how the shapes of the experimental cross-section distributions are reproduced

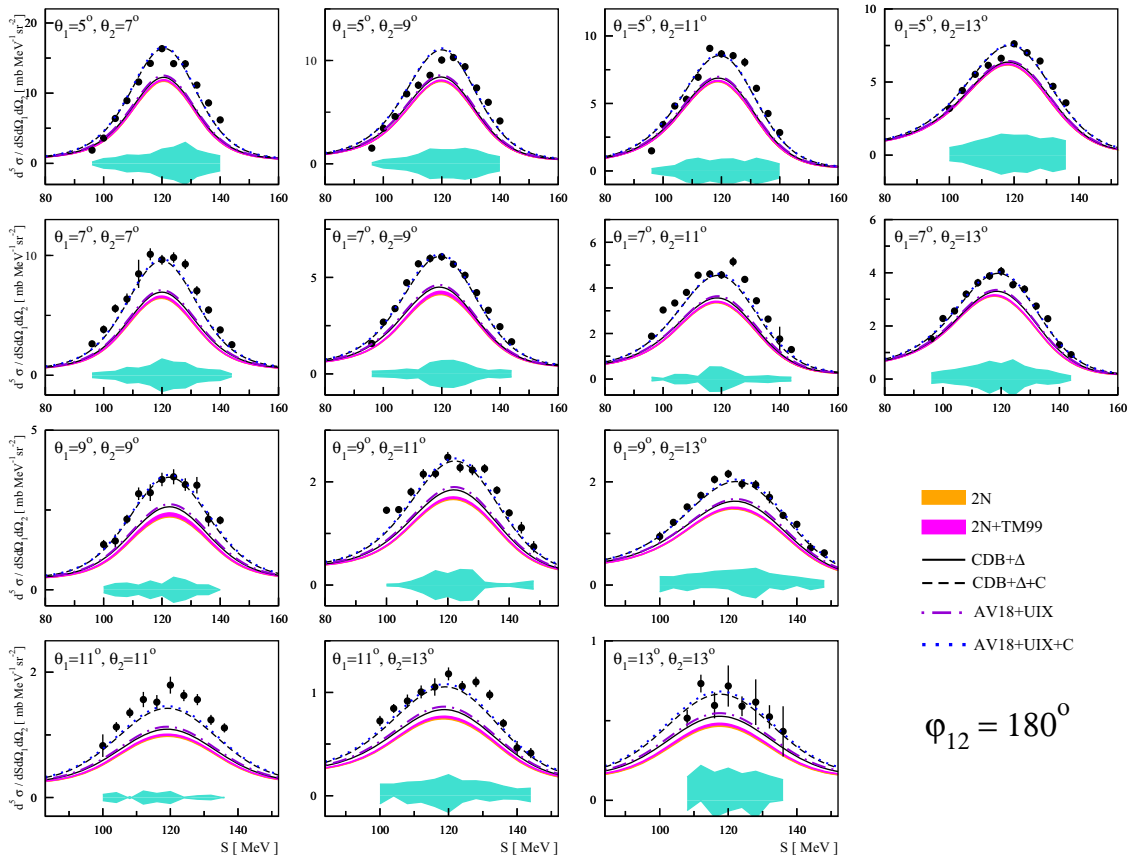

Fig. 18 (Color online) Same as in Fig. 11, but for $\varphi_{12} = 160°$

by different theoretical calculations. In order to avoid biasing of the results with data measured with large systematic uncertainty, which is not included in χ^2 calculations, only the data points with uncertainty of below 30 % are accepted for the χ^2 analysis. The number of the cross-section data points which were rejected due to this condition is about 130.

The data D_i with statistical errors σ_i were compared to the theoretical predictions T_i^m from each type of the model m = 2N, 2N+TM99,AV18+UIX, AV18+UIX+C, CDB+Δ, CDB+Δ+C, N2LO, N3LO. The χ^2/d.o.f. function is given as follows:

$$\chi^2_m/d.o.f. = \frac{1}{N-1}\sum_{i=1}^{N}\left\{\frac{D_i - T_i^m}{\sigma_i}\right\}^2. \tag{8}$$

The χ^2 values for the results presented as bands were calculated with respect to the center of the band. Table 3 presents the global χ^2 per degree of freedom for the whole data set of the differential cross sections. The $\chi^2/d.o.f.$ values obtained with respect to the theories with the Coulomb interaction included is about 12. The values of $\chi^2/d.o.f.$ obtained with respect to the theories without the Coulomb interaction included are about four (N2LO, N3LO, CDB+Δ, AV18+UIX) and six (2N, 2N+TM99) times larger than for the calculations based on the CDB+Δ+C, AV18+UIX+C potentials. Comparing the numbers presented in Table 3 one notices that the 2N potential combined with the TM99 3NF does not improves the description of the data, at least globally. However, in order to judge the influence of 3NF effects, comparisons to calculations which include the Coulomb force should be made. This is possible if the UIX 3NF or the Δ isobar are taken into account. In these cases the χ^2 values are decreased by about 25 %. In the case of the ChPT approach, no calculations which include the Coulomb force are available. However, the results obtained at N3LO describe the data better than the N2LO predictions. In conclusion, only the theories with the electromagnetic interaction implemented reproduce the experimental cross-section data in a reasonable way. Although the range of phase space studied is dominated by Coulomb effects, nevertheless the results obtained indicate the importance of the 3NF for the description of the data.

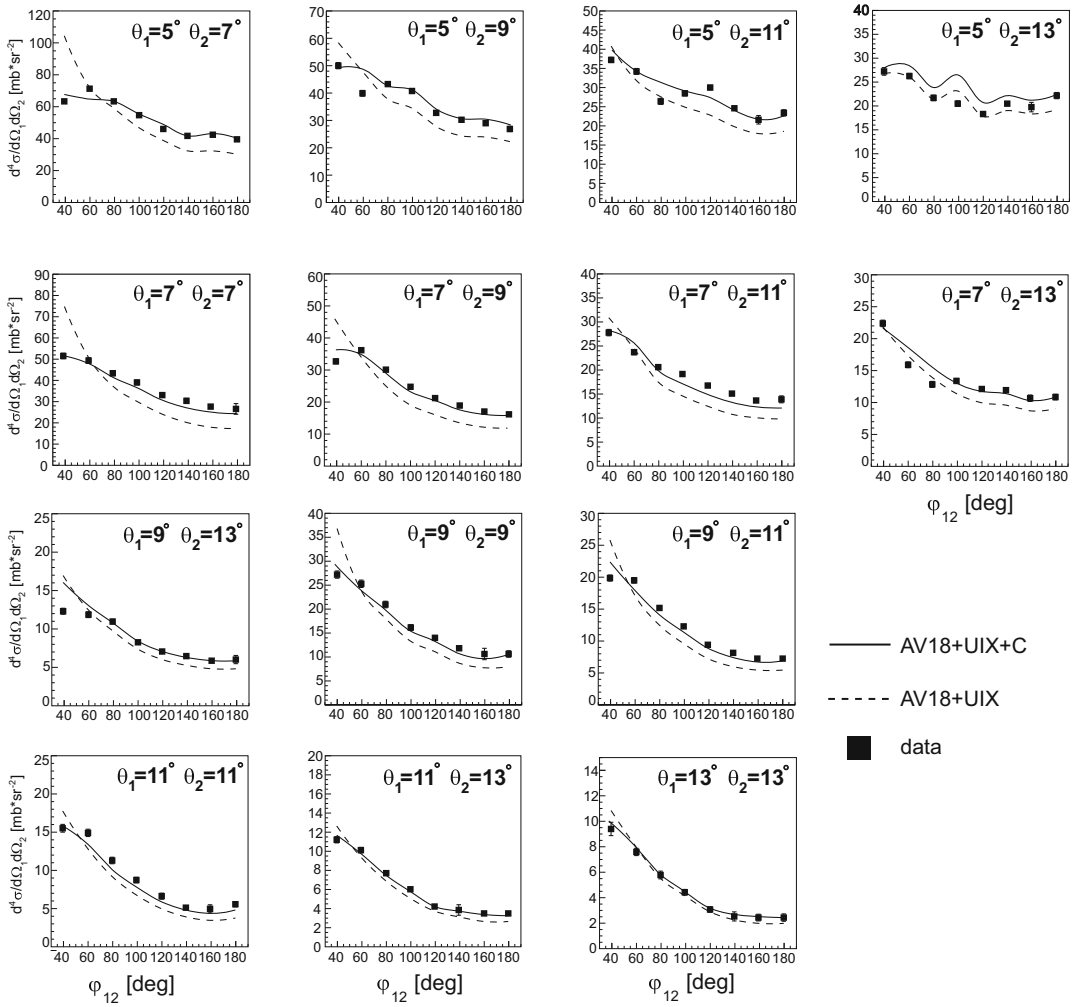

Fig. 19 (Color online) Same as in Fig. 11, but for $\varphi_{12} = 180°$

5.1 Studies of the Data Description Quality

The global features are verified locally with the use of maps of the $\chi^2/d.o.f.$ values, which were calculated for each individual geometrical configuration of the two outgoing protons. This piece of investigation presents comparisons of data integrated over the arc-length variable S with the analogously treated theoretical predictions. Integration of the experimental data is usually straightforward and consists of summing up of events which fulfil the required conditions. Such a procedure requires integration of the theoretical calculations, imposing experimental conditions (e.g. acceptances, thresholds, etc.) to perform reliable comparison with the data. The method is discussed and motivated in [28].

The values of $\chi^2/d.o.f.$ obtained for all configurations are plotted on the θ_1, θ_2 *vs.* φ_{12} plane as colour (gray shading) boxes, see Fig. 20.

The color (gray tint) of each individual box is related to the $\chi^2/d.o.f.$ value for the whole distribution of the observable of interest (summed along S), calculated with respect to a particular theory. The information is similar to the one presented in Fig. 23, but presented in terms of $\chi^2/d.o.f.$ and comprises various theoretical models. In this case the importance of the Coulomb force for the description of the experimental data is also confirmed. As one could expect from the previous analyses, the smallest values of $\chi^2/d.o.f.$ are obtained when the data are compared with the CDB+Δ+C or AV18+UIX+C results and, in general, the same pattern of agreement with data is observed for these two types of predictions. For the calculations which do not take into account the Coulomb force the values obtained for $\chi^2/d.o.f$ are generally very high and can even achieve values as high as 500. There are also configurations given by combinations of thetas: ($\theta_1 = 5°, \theta_2 = 13°$),

Table 3 Global χ^2 per degree of freedom for the experimental cross-section values with respect to different theoretical predictions

Theory	$\chi^2/d.o.f.$
2N	94.1
2N+TM99	93.5
ChPT N2LO	79.8
ChPT N3LO	66.2
CDB+Δ	68.4
CDB+Δ+C	12.3
AV18+UIX	64.4
AV18+UIX+C	11.9
AV18+C	12.3

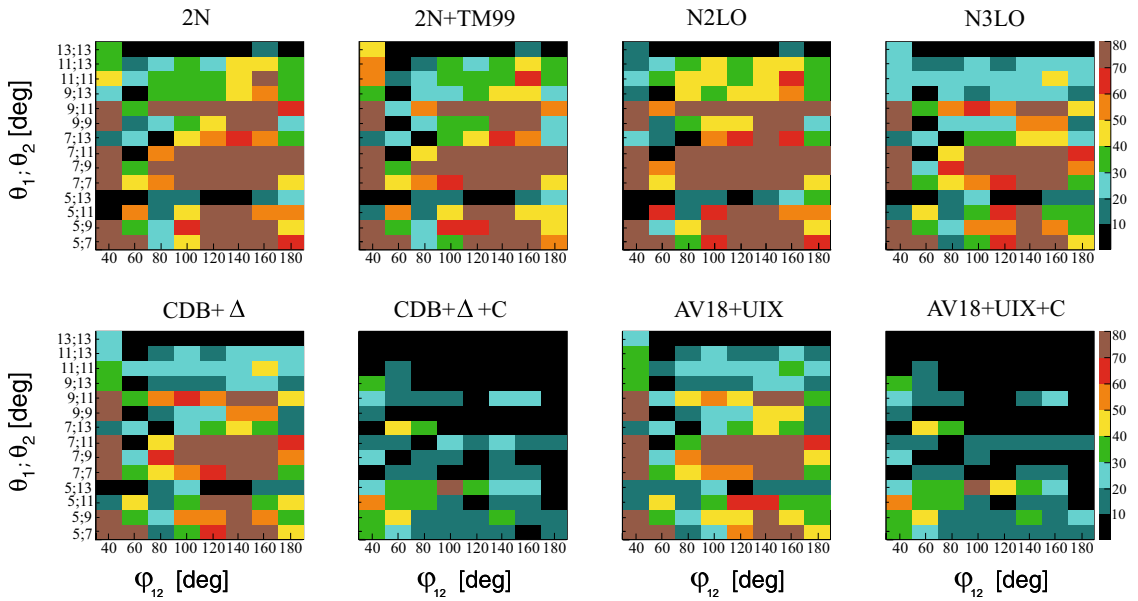

Fig. 20 (Color online) Set of $\chi^2/d.o.f.$ maps, obtained for the differential cross sections and compared to various theoretical predictions

($\theta_1 = 7°, \theta_2 = 13°$), ($\theta_1 = 13°, \theta_2 = 13°$), where predictions of all theoretical calculations are consistent with each other over the whole arc-length range. For these particular geometries the calculations do not reveal sensitivity to any effects or those effects cancel and the net effect is negligible.

There are regions of the phase space where the predictions with the Coulomb interaction incorporated in the dynamics differ dramatically from the ones without this piece of the dynamics. The most pronounced Coulomb force manifestation is observed for very small polar and relative azimuthal angles between the two outgoing protons. This is particularly true for $\varphi_{12} = 40°$ (the lowest relative azimuthal angle accessible in this experiment). In this case the Coulomb interaction leads not only to a strong suppression of the cross section, but also to a distortion of the distribution.

To search for possible regularities in changes of the quality of the data descriptions by the models, the consistency between the data and the theories were studied via inspection of the dependence of $\chi^2/d.o.f.$ on the kinematical variables, like relative azimuthal angle φ_{12} of the proton from the breakup reaction, pair of the polar angles of the two protons θ_1, θ_2 and the energy of the relative motion of the two protons E_{12}.

In the first case the χ^2/d.o.f. values have been calculated as in the global χ^2 analysis, but for groups of configurations defined by the same φ_{12} value (Fig. 21). The values of χ^2/d.o.f. obtained for Coulomb-containing predictions are in the range of 2–20, whereas for the rest of the theories vary between 30 and 100, reaching the highest values of 300–400 for $\varphi_{12} = 40°$. At this relative azimuthal angle, the effect of the Coulomb force is the strongest, in contrary to $\varphi_{12} = 60°$, at which the net effect of the electromagnetic component is negligible. Among the other theoretical predictions one can distinguish two groups: (2N, 2N+TM99, N2LO) and (CDB+Δ, AV18+UIX, N3LO), which provide slightly different, but generally large values of $\chi^2/d.o.f.$. Note that the calculations at N3LO presented here do not contain the chiral 3NF, therefore, the $\chi^2/d.o.f.$ analysis for this

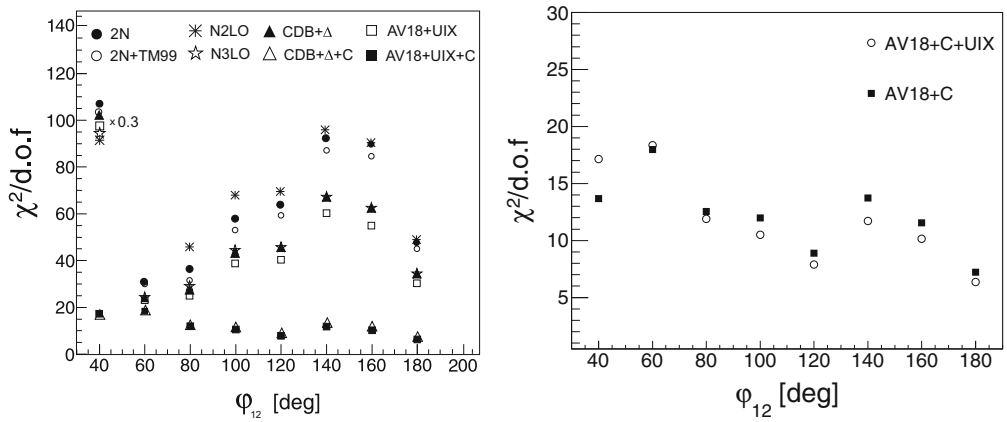

Fig. 21 *Left panel* : Quality of description of the cross-section data with various theoretical predictions (defined in the legend), expressed as dependence of $\chi^2/d.o.f.$ on the relative azimuthal angle φ_{12}. Points with very large $\chi^2/d.o.f.$ values are scaled down by factors indicated in the panels. Points corresponding to Coulomb-containing predictions almost overlap. For clarity, they are presented separately in zoomed-in scale (*rigth panel*)

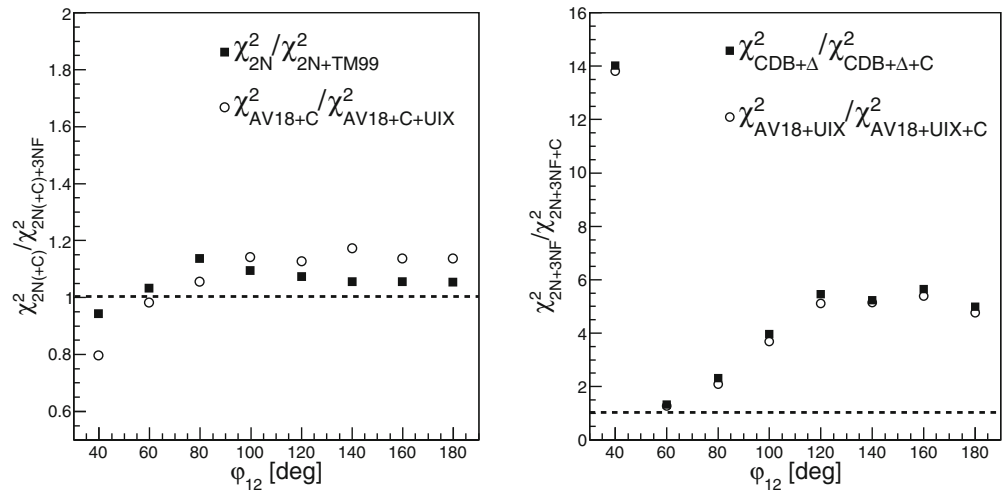

Fig. 22 *Left panel* : Ratios of χ^2 values for predictions without and with 3NF contributions calculated for groups of kinematical configurations with the same φ_{12}. *Right panel* : same calculations, but with respect to the Coulomb force contribution

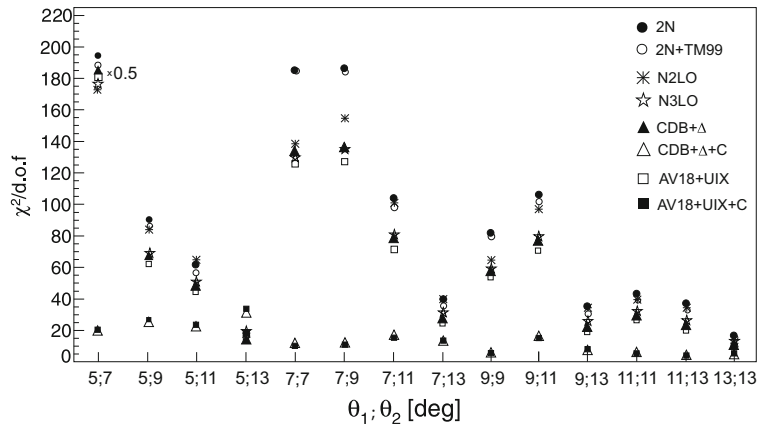

Fig. 23 Quality of description of the cross-section data with various theoretical predictions (defined in the legend), expressed as dependence of $\chi^2/d.o.f.$ on the combination of the proton emission polar angles. Points with very large $\chi^2/d.o.f.$ values are scaled down by factors indicated in the *panels*

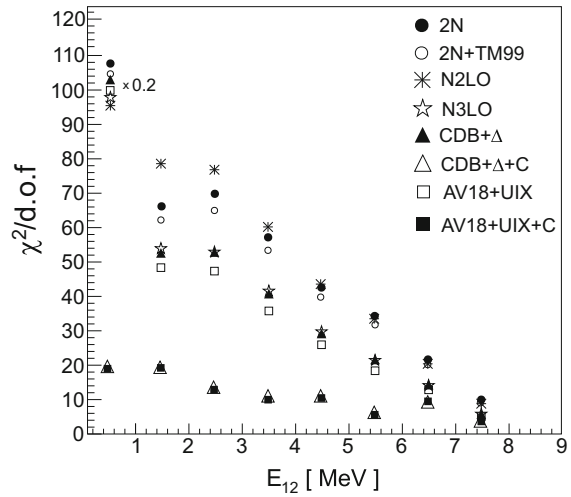

Fig. 24 Quality of description of the cross-section data with various theoretical predictions (defined in the legend), expressed as dependence of $\chi^2/d.o.f.$ on the relative energy of the two protons from the breakup reaction E_{12}. Points with very large $\chi^2/d.o.f.$ values are scaled down by factors indicated in the panels

case should be treated with caution. Effects of the 3NF and Coulomb interactions are magnified by calculating ratios of χ^2, as presented in Fig. 22. The calculations including 3NF effects provide a better description of the data in the region of $\varphi_{12} > 60°$.

The dependence of $\chi^2/d.o.f.$ on different combinations of θ_1, θ_2 (see Fig. 23) was also checked. With increasing $\Delta\theta = \mid \theta_1 - \theta_2 \mid$ value the Coulomb effects play a less important role in reproducing the experimental data and for high $\Delta\theta$ all theories predict almost the same values for the cross sections.

The χ^2 dependence on the energy of the relative motion of the two protons E_{12} was also studied. One can expect that the Coulomb force between the protons plays a crucial role for small E_{12}, corresponding to proton–proton FSI configurations. The results (see Fig. 24) confirms the expectation: in the case of small values of E_{12} the Coulomb effects are extremely large and disagreement between the experimental data and theoretical predictions without the Coulomb force included decreases with increasing relative energy. For very large $E_{12} \geq 6.5$ MeV the discrepancies are still present, but become much smaller. This range of E_{12} corresponds to a quick separation of the two protons, and therefore, is less sensitive to the electromagnetic interaction.

6 Summary and Outlook

The experimental investigation of the ^{1}H(**d**, pp)n breakup reaction at 130 MeV in the forward angular region was mostly devoted to the study of Coulomb force effects, since the theoretical calculations predict a very significant influence of the electromagnetic interaction in the part of the phase space studied. Therefore, the differential cross sections $\frac{d^5\sigma}{d\Omega_1 d\Omega_2 dS}$ for 121 geometries have been obtained, which constitute a database of about 1700 experimental points. The data complement the earlier experimental studies at this energy, which explored the phase space region sensitive to 3NF effects, but also demonstrated, for the first time, the significant influence of the Coulomb interaction on the cross-section data [27–29]. The data presented in this paper are a unique basis to test modern approaches of including the Coulomb interaction in calculations of the 3N system. The study of the most sensitive region of the phase space which is characterized by geometries with very small relative azimuthal angles of $\varphi_{12} = 20°$ turned out to be impossible. This was due to the fact that the corrections for the inefficiency caused by the detector granularity were too high. There are a few configurations defined by 5° (edge of the detector acceptance) for which the cross-section values are strongly affected by large systematic uncertainties. The source of the errors was the large background contribution caused by the effect of the beam tail on the detector at the lowest θ angles. However, there is still a large number of 80 geometries for which the absolute values of the cross sections are not biased by large systematic uncertainties.

The models with the Coulomb interaction included (i.e. CD Bonn+Δ+C, AV18+UIX+C) reproduce the present data in a consistent way. The results obtained in the χ^2/d.o.f. analysis confirm the necessity for inclusion

of the electromagnetic interaction into the calculations in order to assure reasonable agreement between the theoretical models and the experimental data.

The magnitude of the predicted 3NF effects in the region of the phase space studied depends on the approach. For the coupled-channel potential CD Bonn + Δ the effect of the Δ-isobar excitation is rather moderate and of the same order as for the Argonne V18 potential supplemented by the Urbana IX 3NF. In the case of the TM99 3NF the effects are practically negligible. The ChPT predictions also reveal moderate contributions of the 3NF effects. The N3LO calculations (presently available with NN contributions only) describe the data in a better way than at N2LO. Both are characterised by a broad range of the predicted cross-section values. Recently, a new generation of chiral NN potentials up to N4LO has been developed [50]. Equipped with a new approach for quantifying the theoretical uncertainty by means of estimating the size of higher-order contributions, the new NN potentials were shown to provide accurate results for NN scattering observables up to E_{lab} = 200 MeV. The study of the deuteron breakup reaction within this approach is envisioned. Although the 3NF effects are small in the phase-space region studied, their contribution to the dynamics is not negligible and is of importance in studies of the 3N dynamics.

The study presented makes an important step towards a complete description of the breakup observables, confirming the large sensitivity of the breakup cross-section to the Coulomb force in the very forward angular region. Currently available theoretical approaches which model the interaction require a very precise and large experimental database for their verification and further development. Within these predictions different elements of the dynamics can be studied separately as well as their mutual interplay. There is still a strong need for the complete theoretical treatments which include all the ingredients of the 3N dynamics: 3NF effects, Coulomb interaction as well as relativistic effects.

Acknowledgments This work was partially supported by the Polish science funds as research Projects No. N N202 174635 (2008–2010) and No. 2012/05/E/ST2/02313 (2013–2016). This study was also supported by the Polish National Science Center under Grant No.DEC-2013/10/M/ST2/00420. The numerical calculations of the Cracow-Bochum group have been performed on the supercomputer clusters of the JSC, Jülich, Germany.

References

1. Yukawa, H.: On the interaction of elementary particles. Proc. Phys. Math. Soc. Jap. **17**, 48 (1935)
2. Wiringa, R.B. et al.: Accurate nucleon-nucleon potential with charge-independence breaking. Phys. Rev. C **51**, 38–51 (1995)
3. Machleidt, R. et al.: The non-local nature of the nuclear force and its impact on nuclear structure. Phys. Rev. C **53**, 1483 (1996)
4. Stoks, V.G.J. et al.: Construction of high quality NN potential models. Phys. Rev. C **49**, 2950–2962 (1994)
5. Deltuva, A., Chmielewski, K., Sauer, P.U.: Nucleon deuteron scattering with delta-isobar excitation: Chebyshev expansion of two baryon transition matrix. Phys. Rev. C **67**, 034001 (2003)
6. Deltuva, A., Machleidt, R., Sauer, P.U.: Realistic two-baryon potential coupling two-nucleon and nucleon-Δ-isobar states: fit and applications to three-nucleon system. Phys. Rev. C **68**, 024005 (2003)
7. Epelbaum, E. et al.: Three nucleon forces from chiral effective field theory. Phys. Rev. C **66**, 064001 (2002)
8. Epelbaum, E. et al.: Improving the convergence of the chiral expansion for nuclear forces. 1. Peripheral phases. Eur. Phys. J. A **19**, 125–137 (2004)
9. Nogga, A. et al.: The three nucleon bound state using realistic potential models. Phys. Rev. C **67**, 034004 (2003)
10. Witala, H. et al.: The cross-section minima in elastic Nd scattering: a 'smoking gun' for three nucleon force effects. Phys. Rev. Lett. **81**, 1183–1186 (2003)
11. Nemoto, S. et al.: Discrepancy in the cross section minimum of elastic nucleon-deuteron scattering. Phys. Rev. C **58**, 2599–2602 (1998)
12. Sakai, H. et al.: Precise measurement of dp elastic scattering at 270 MeV and three-nucleon force effects. Phys. Rev. Lett. **84**, 5288–5291 (2000)
13. Ermisch, K. et al.: Search for three-nucleon force effects in analyzing powers for p-d elastic scattering. Phys. Rev. Lett. **86**, 5862–5865 (2001)
14. Cadman, R.V.: Evidence for a three-nucleon-force effect in proton-deuteron elastic scattering. Phys. Rev. Lett. **86**, 967–970 (2001)
15. Hatanaka, K. et al.: Cross-section and complete set of proton spin observables in p polarized d elastic scattering at 250-MeV. Phys. Rev. C **66**, 044002 (2002)
16. Ermisch, K. et al.: Systematic investigation of the elastic proton deuteron differential cross-section at intermediate-energies. Phys. Rev. C **68**, 051001 (2003)
17. Sekiguchi, K. et al.: Polarization transfer measurement for H-1(polarized-d, polarized-p) H-2 elastic scattering at 135-MeV/u and three nucleon force effects. Phys. Rev. C **70**, 014001 (2004)
18. Mermod, P. et al.: Search for three-body force effects in neutron-deuteron scattering at 95 MeV. Phys. Lett. B **597**, 243–248 (2004)
19. Pudliner, B.S. et al.: Quantum Monte Carlo calculations of nuclei with A<7. Phys. Rev. C **56**, 1720 (1997)
20. Coon, S.A., Han, H.K.: Reworking the Tucson-Melbourne three-nucleon potential. Few-Body Syst. **30**, 131 (2001)
21. Fujita, J., Miyazawa, H.: Pion theory of three-body forces. Prog. Theor. Phys. **17**, 360 (1957)

22. Entem, D.R., Machleidt, R.: Accurate nucleon-nucleon potential based upon chiral perturbation theory. Phys. Lett. B **524**, 93–98 (2002)
23. Epelbaum, E.: Few-nucleon forces and systems in chiral effective field theory. Prog. Part. Nucl. Phys. **57**, 645–741 (2006)
24. Skibiński, R. et al.: Triton with long-range chiral N^3LO three-nucleon forces. Phys. Rev. C **84**, 054005 (2011)
25. Golak, J. et al.: Low-energy neutron-deuteron reactions with N^3LO chiral forces. Eur. Phys. J A **50**, 177 (2014)
26. Witała, H., Golak, J., Skibiński, R., Topolnicki, K. et al.: Calculations of three-nucleon reactions with N^3LO chiral forces: achievements and challenges. J. Phys. G: Nucl. Part. Phys. **41**, 1–22 (2014)
27. Kistryn, St. et al.: Evidence of three-nucleon force effects from 130 MeV deuteron-proton breakup cross section measurement. Phys. Rev. C **68**, 054004 (2003)
28. Kistryn, St. et al.: Systematic study of three-nucleon force effects in the cross section of the deuteron-proton breakup at 130 MeV. Phys. Rev. C **72**, 044006 (2005)
29. Kistryn, St. et al.: Evidence of the Coulomb-force effects in the cross sections of the deuteron-proton breakup at 130 MeV. Phys. Lett. B **641**, 23–27 (2006)
30. Ciepał, I. et al.: Studies of the three-nucleon system dynamics in the deuteron-proton breakup reaction. EPJ Web of Conferences **37**, 09011 (2012)
31. Ciepał, I. et al.: Investigations of few-nucleon system dynamics in medium energy domain. Few-Body Sys. **601**, 1–5 (2013)
32. Deltuva, A., Fonseca, A.C., Sauer, P.U.: Momentum-space treatment of the Coulomb interaction in the three-nucleon reactions with two protons. Phys. Rev. C **71**, 054005 (2005)
33. Deltuva, A., Fonseca, A.C., Sauer, P.U.: Momentum-space description of three-nucleon breakup reactions including the Coulomb interaction. Phys. Rev. C **72**, 054004 (2005)
34. Deltuva, A., Fonseca, A.C., Sauer, P.U.: New calculations schemes for proton-deuteron scattering including the Coulomb interaction. Phys. Rev. C **73**, 057001 (2006)
35. Deltuva, A.: Momentum-space calculation of proton-deuteron scattering including Coulomb and irreducible three-nucleon forces. Phys. Rev. C **80**, 064002 (2009) [E. Epelbaum, H. Krebs, U.-G Meiner, arXiv:1412.4623 [nucl-th]]
36. Eslami-Kalantari, M. et al.: Measurements of scattering observables for the pd break-up reaction. EPJ Web Conf. **3**, 05010 (2010)
37. Kalantar-Nayestanaki, N. et al.: Signatures of three-nucleon interactions in few-nucleon systems. Rep. Prog. Phys. **75**, 016301 (2012)
38. Stephan, E. et al.: Vector and tensor analyzing powers in deuteron-proton breakup at 130 MeV. Phys. Rev. C **82**, 014003 (2013)
39. Stephan, E. et al.: Vector analyzing powers of the deuteron-proton elastic scattering and breakup at 100 MeV. Eur. Phys. J. A **49**, 36 (2013)
40. Ciepał, I. et al.: Vector analyzing powers of deuteron-proton elastic scattering and breakup at 130 MeV. Phys. Rev. C **85**, 017001 (2012)
41. Maier, R.: Cooler synchrotron COSY—performance and perspectives. Nucl. Instr. Meth. in Phys. Res. A **390**, 1 (1997)
42. Jaeckle, V. et al.: A Liquid hydrogen/deuterium target with very thin windows. Nucl. Instrum. Meth. A **349**, 15–17 (1994)
43. Hassan, A. et al.: A multifunctional cryo-target for the external COSY experiments. Nucl. Instrum. Meth. A **425**, 403–408 (1999)
44. Betigeri, M. et al.: The germanium wall of the GEM detector system. Nucl. Instrum. Meth. A **421**, 447–457 (1999)
45. Żołnierczuk, P.A., Garske, W.: Data analysis software for gem experiments at COSY. GEM Internal Report (1998)
46. Garske, W.: Untersuchung der π^0 und π^+ Produktion in Proton-Proton und Proton-Deuterium Wechselwirkung bei 850 MeV/c, Münster University (1999)
47. http://www.srim.org/
48. Shimizu, H. et al.: Analysing Powers and Cross Sections in Elastic p-d Scattering at 65 MeV. Nucl. Phys. A **382**, 242 (1982)
49. Epelbaum, E., Krebs, H., Meißner, U.-G.: Improved chiral nucleon-nucleon potential up to next-to-next-to-next-to-leading order, arXiv:1412.0142 [nucl-th] (2014)
50. Epelbaum, E., Krebs, H., Meißner, U.-G.: Precision nucleon-nucleon potential at fifth order in the chiral expansion, arXiv:1412.4623 [nucl-th] (2014)
51. Faddeev, L.D.: Scattering theory for three particle system. Sov. Phys. JETP **12**, 1014 (1961)